Atmospheric
Measurement
Techniques

Open Access

Discussions

EGU

1 **Characterisation of the filter inlet system on the BAE-146 research aircraft and its use for size**
2 **resolved aerosol composition measurements**

3 Alberto Sanchez-Marroquin[1], Duncan H. P. Hedges[1], Matthew Hiscock[2], Simon T. Parker[3], Philip D. Rosenberg[1], Jamie
4 Trembath[4], Richard Walshaw[1], Ian T. Burke[1], James B. McQuaid[1], Benjamin J. Murray[1]

5 [1]School of Earth and Environment, University of Leeds, Woodhouse Lane, Leeds, LS2 9JT, UK
6 [2] Oxford Instruments NanoAnalysis, High Wycombe, HP12 3SE
7 [3]Defence Science and Technology Laboratory, Salisbury, SP4 0JQ, UK
8 [4]Facility for Airborne Atmospheric Measurements, Building 146, Cranfield University, College Road, Cranfield, Bedford
9 MK43 0AL

10

11 **Abstract**

12 Atmospheric aerosol particles are important for our planet's climate because they interact with
13 radiation and clouds. Hence, having characterised methods to collect aerosol from aircraft for detailed
14 offline analysis are valuable. However, collecting aerosol, particularly coarse mode aerosol, onto
15 substrates from a fast moving aircraft is challenging and can result in both losses and enhancement in
16 aerosol. Here we present the characterisation of an inlet system designed for collection of aerosol
17 onto filters on board the UK's BAe 146 Facility for Airborne Atmospheric Measurements (FAAM)
18 research aircraft. We also present an offline Scanning Electron Microscopy (SEM) technique for
19 quantifying both the size distribution and size resolved composition of the collected aerosol. We use
20 this SEM technique in parallel with online underwing optical probes in order to experimentally
21 characterise the efficiency of the inlet system. We find that the coarse mode aerosol is sub-
22 isokinetically enhanced, with a peak enhancement at around 10 µm up to a factor of three under
23 typical operating conditions. Calculations show that the efficiency of collection then decreases rapidly
24 at larger sizes. In order to minimise the isokinetic enhancement of coarse mode aerosol we
25 recommend sampling with total flow rates above 50 L min⁻¹; operating the inlet with the bypass fully
26 open helps achieve this by increasing the flow rate through the inlet nozzle. With the inlet
27 characterised, we also present single particle chemical information obtained from X-ray spectroscopy
28 analysis which allows us to group the particles into composition categories. Our intention is to use the
29 composition information in parallel with filter based ice nucleating particle measurements in order to
30 correlate composition and ice nucleating particle concentrations.

31

Atmospheric
Measurement
Techniques
Discussions

1 Introduction

Atmospheric aerosol particles are known to have an important effect on climate through directly scattering or absorbing solar and terrestrial radiation as well as through indirect effects such as acting as Cloud Condensation Nuclei (CCN) or Ice-Nucleating Particles (INPs) (Albrecht, 1989; DeMott et al., 2010; Haywood and Boucher, 2000; Hoose and Mohler, 2012; Lohmann and Diehl, 2006; Lohmann and Gasparini, 2017). Aerosol particles across the fine (diameter < 2 µm) and coarse (>2 µm) modes are important for these atmospheric processes. For example, aerosol in the accumulation mode are important CCN (Seinfeld and Pandis, 2006), whereas supermicron particles are thought to contribute substantially to the INP population (Mason et al., 2016; Pruppacher and Klett, 1997) Hence, being able to sample across the fine and coarse modes is required to understand the role aerosol play in our atmosphere. However, sampling aerosol particles without biases can be challenging, this being especially so on a fast moving aircraft (Baumgardner et al., 2011; Baumgardner and Huebert, 1993; McMurry, 2000; Wendisch and Brenguier, 2013).

It is necessary to sample aerosol from aircraft because in many cases aircraft offer the only opportunity to study aerosol and aerosol-cloud interactions at cloud relevant altitudes (Wendisch and Brenguier, 2013). However, the relatively high speeds involved present a set of unique challenges for sampling aerosol particles. This is especially so for coarse mode aerosol which are prone to both losses as well as enhancements because their high inertia inhibits their ability to follow the air stream lines when they are distorted by the aircraft fuselage and the inlet (Brockmann, 2011; McMurry, 2000; von der Weiden et al., 2009). Therefore, inlet design and characterisation becomes extremely important when sampling aerosol particles.

In this study we characterise the inlet system used for collecting filter samples (known as the Filters system) on board the UK's BAe 146 Facility for Airborne Atmospheric Measurements (FAAM) research aircraft. This system has been used for many years, but its characterisation has been limited. Our goal in this characterisation work was to define recommendations for the use of the inlet system to minimise sampling biases and define the size limitation and the biases that exist. While the filter samples could be used for a variety of offline analyses, we have done this characterisation with two specific goals in mind: firstly, we want to use this inlet system for quantification of INP (the technique for this analysis has been described previously (Price et al., 2018) and will not be further discussed here); secondly, we have adapted and developed a technique for quantification of size distributions and size resolved composition using Scanning Electron Microscopy (SEM). We use the SEM derived size distributions in comparison with the size distributions obtained from the underwing probes to experimentally test the inlet efficiency. These experiments are underpinned by calculations which elucidate how the biases are impacted by variables such as flow speed, angle of attack and use of the bypass system. Finally we present an example of the use of the inlet for determining the size resolved composition of an aerosol sample collected from the FAAM aircraft.

2. Description and theoretical sampling characteristics of the filter inlet system on the Facility for Airborne Atmospheric Measurements (FAAM) aircraft

Ideally, aerosol particles would be sampled through inlets without enhancement or losses. However, this is typically not the case when sampling from aircraft, hence it is important to know how the size distribution of the aerosol particles is affected by the sampling. Generally, an aircraft moves at high velocities with respect to the air mass that it is being sampled. During sampling on the FAAM aircraft the indicated airspeed is 100 m s^{-1}, which yields to a true airspeed that fluctuates between 100 and 120 m s^{-1}. The air mass has to decelerate when passing through the inlet (Baumgardner and Huebert, 1993) and this tends to result in inertial enhancement of coarse mode aerosol. There are also losses

Atmospheric
Measurement
Techniques
Discussions

77   through the inlet system, for example, through inertial impaction at bends or gravitational settling in

78   horizontal sections of pipework. These inlet characteristics need to be considered if the subsequent

79   analysis of the aerosol samples is to be quantitative. In this section we first describe the existing inlet

80   system and then present theoretical calculations for the size dependent losses and enhancements.

81   **2.1 Description of the Filters system**

82   The UK's FAAM BAe-146 research aircraft has two identical inlets for sampling aerosol onto filters for

83   offline analysis. This inlet system was used to sample aerosol particles on board of the C-130 aircraft

84   before being installed on the FAAM Bae-146 (Andreae et al., 1988; Andreae et al., 2000; Talbot et al.,

85   1990), and it has been used to sample aerosol particles on the FAAM Bae-146 e.g. (Chou et al., 2008;

86   Hand et al., 2010; Price et al., 2018; Young et al., 2016). A diagram of the inlet system can be seen in

87   Fig. 1. The two parallel inlet and filter holder systems, which each have a nozzle whose leading edge

88   profile follows the criteria for aircraft engine intakes at low Mach numbers (low speeds when

89   compared with the speed of sound; for FAAM during sampling this is ~0.3), and it is designed to avoid

90   the distortion of the pressure field at the end of the nozzle, flow separation and turbulence (Andreae

91   et al., 1988). The inlet has a bypass to remove water droplets or ice crystals through inertial separation

92   and also enhance the flow rate at the inlet nozzle (Talbot et al., 1990). The flow through the bypass

93   (bypass flow) can be regulated using a valve and it is driven passively by the pressure differential

94   between the ram pressure inlet and the Venturi effect on the exhaust. After turning inside the aircraft,

95   the airstream containing the aerosol particles continue through the filter stack after passing a valve.

96   The air flow through the filter (filter flow) is measured by a mass flow meter, which reports the

97   standard litres sampled (273.15 k, 1013.529 hPa). The signal is integrated by an electronics unit to give

98   the total volume of air sampled for any given time period. There is also a valve between the pump and

99   the flow meter. The valve allows the inlet and pump to be isolated from the filter holder when

100   changing the filter. The system uses a double-flow side channel vacuum pump model SAH55 made by

101   Rietschie, aided by the ram effect of the aircraft. The flow rate at the inlet nozzle (total flow) is the

102   sum of the bypass flow and the filter flow. The inlet nozzle is located at 19.5 cm of the aircraft fuselage,

103   so the sampling is carried out in the free stream, outside the boundary layer.

104

105   **2.2 Sampling efficiency**

106   We present theoretical estimates of the losses and enhancements due to aspiration, inlet inertial

107   deposition, turbulent inertial deposition, inertial deposition in bends and gravitational effects in Fig

108   2a. We used the term 'efficiency' to define the ratio between the number concentrations of particles

109   after they were perturbed relative to the unperturbed value. If the efficiency is above one, the number

110   of particles is enhanced whereas if it is below 1, particles are lost.

111   The sampling efficiency of any inlet depends strongly on the flow rates and the flow regime (laminar

112   vs turbulent). Filter flow rates for 0.4 µm polycarbonate filters normally vary between 10 and 50 L min^{-1}

113   depending on altitude (see section 2.3 for a discussion of flow rates). The bypass flow rate (when it

114   is fully open) can go up to 35 L min^{-1} at 30 m and 22 L min^{-1} at 6 km, but it is not measured routinely.

115   In the 2.5 cm diameter section of the inlet, the Reynolds number (Re) is below the turbulent regime

116   threshold (Re > 4000) for flow rates below 65 L min^{-1}. For larger values of Re, the flow starts becoming

117   turbulent. At the inlet nozzle, where the diameter 0.7 cm, Re is above 4000 for flow rates above 20 L

118   min^{-1}, so the flow is briefly in the turbulent regime at the inlet for most sampling conditions. Fully

119   characterising the losses and enhancements of aerosol particles passing through the inlet is very

120   challenging since there are several aerosol size dependent mechanisms than can enhance or diminish
121   the amount of aerosol particles that arrive at the filter.

122   Here we have considered the most important of these mechanisms in order to estimate the inlet
123   efficiency (see Fig. 2a) for a total flow rate of 50 L min^{-1}. These loss mechanisms and their importance
124   in this inlet system are defined as follows (a discussion on the choice of equations and how they have
125   been applied can be found in Appendix A):

126   *Aspiration efficiency* accounts for the fact that the speed of the sampled air mass (U_0) and the speed
127   of the air through the beginning of the inlet nozzle (U) are different. In the case of the filter inlet
128   system on the FAAM aircraft, the speed of the air mass is greater than the speed through the inlet
129   (sub-isokinetic conditions), which leads to an enhancement of larger aerosol particles. Here, we have
130   used the empirical equation as develop in Belyaev and Levin (1972) and Belyaev and Levin (1974). As
131   one can see in Fig. 2a this mechanism enhances aerosol particles, tending to 1 for small diameters and
132   to the ratio U/U_0 for large ones.

133   *Inlet inertial deposition* is the inertial loss of aerosol particles within the nozzle because the flow
134   expands inside the nozzle and the trajectory is therefore bent towards the wall. It has been
135   characterised using the equation given in Liu et al. (1989) which quantifies this effect. In Fig. 2a one
136   can see that it produces some losses, with a minimum efficiency of down to 50% for sizes about 6 μm,
137   without affecting the lower and upper limit of the aerosol size.

138   *Turbulent inertial deposition* happens when some particles are collected by the wall due to
139   turbulences in the system. In our case, this occurs throughout the whole inlet system for flow rates
140   above 65 L min^{-1} and only occurs in the inlet nozzle for flow rates below this threshold. We have used
141   the equation given by Brockmann (2011) in order to account for this mechanism, which can be seen
142   in Fig. 2a. This mechanism gradually decreases the efficiency for aerosol particles above 5 μm.

143   *Bending inertial deposition* of aerosol particles is important in this inlet system at the 45° bend, where
144   some particles are not able to follow air streamlines at bend. We have characterised these losses using
145   the equation given in (Brockmann, 2011). This efficiency mechanism, which can be seen in Fig. 2a,
146   adds a size cut off with a D50 value at ~25 μm.

147   *Gravitational settling* of aerosol particles was considered using the equations developed in Heyder
148   and Gebhart (1977) and Thomas (1958), as stated in Brockmann (2011). This efficiency mechanism
149   adds another size cut off with a D50 value of 35 μm, as one can see in Fig. 2a.

150   *Diffusional efficiency and filter collection efficiency* have not been included in Fig. 2. The first
151   mechanism has been calculated using the analytical equation given by Gormley and Kennedy (1948),
152   but it is not shown since it is very close to 1 for all the considered size range. For the filter types and
153   pore sizes we used, filter collection efficiency is also close to a 100% across the relevant size range
154   (Lindsley, 2016; Soo et al., 2016).

155   *Anisoaxial losses* are losses produced by the fact that the inlet is not aligned with the velocity of the
156   air mass, being offset by an angle, θ (related to the angle of attack). The anisoaxial sampling can affect
157   the sub-isokinetic efficiency, but using the equations given by Hangal and Willeke (1990a), we
158   calculated that this effect is minimal for our conditions. In addition, anisoaxial sampling can lead to
159   inertial losses when particles impact the inner walls of the inlet. This phenomena has been quantified
160   using the equations in Hangal and Willeke (1990b) and the results can be seen in Fig. 3. As one can
161   see, this efficiency mechanism adds an additional cut off for large aerosol particles (with values of D50
162   down to ~20 μm), depending on the value of the sampling angle.

Atmospheric
Measurement
Techniques
Discussions

163   One can see all the efficiency mechanisms combined for four different flow rates in Fig. 2b. These have
164   been derived by multiplying all the efficiencies for the individual mechanisms. This overall efficiency
165   is the ratio between the particles that reach the filter and the particles in the ambient air. The
166   sampling efficiency for the submicron aerosol is close to 1. At sizes above 1 μm, the different loss
167   mechanisms become increasingly significant. For the range of flow rates considered, the efficiency
168   approaches zero between 20 and 50 μm, with D50 values in between ~13 and ~33 μm (although these
169   values could be lower under certain values of angles of attack if considering the anisoaxial losses of
170   from Fig. 3, which haven't been included). For the 80 L min^{-1} case, the flow is turbulent through all the
171   pipe, leading to enhanced losses of coarse aerosol particles which partially compensate the sub-
172   isokinetic enhancement of the system.

173   One can also see that the sub-isokinetic enhancement of large aerosol particles increases when
174   decreasing the flow rate of the system. This effect is about a factor 3.5 for 10 μm particles when
175   sampling at 15 L min^{-1}, but only a factor of two at 50 L min^{-1}. The sub-isokinetic enhancement can be
176   mitigated using the bypass, which enhances the flow through the nozzle. This can be seen in Fig. 2c
177   where one can see a comparison between the total efficiency of a 20 L min^{-1} flow rate through the
178   filters with no bypass flow and the same case when the bypass is open. Since the considered bypass
179   flow is comparable to the flow rate through the filters, the difference between the total flows for the
180   two cases is approximately a factor 2. As a consequence, the maximum sub-isokinetic enhancement
181   of large aerosol particles is almost a factor 2 larger when sampling with the bypass closed. Hence, the
182   sub-isokinetic enhancement can be reduced by keeping the bypass fully open.

183

184   2.3 Sampling flow rate

185   Here we show flow rate data from four field campaigns in order to examine how the flow rate of the
186   filter inlet system varied based on different factors. We have used the data collected during the ICE-D
187   campaign, in Cape Verde during August 2015 (Price et al., 2018). The rest of the data is from some
188   flight test carried out during 2017 and 2018, and three field campaigns. The first one was EMERGE,
189   based in south east England, in July 2017. The second one was VANAHAEIM, based in Iceland in
190   October 2017. The last campaign was MACSSIMIZE, based in Alaska in 2018. The flow rate of the inlet
191   system is known to vary with altitude, with a lower flow rate at high altitudes because of the reduced
192   pressure differential across the filter and the fact that the pump efficiency decreases at low pressure.
193   In addition, it changes depending on the filter type and the pore size.

194   In Fig. 4, where all the flow rate data has been presented, one can see that the flow rate tends to
195   decrease with altitude and change with filter type as expected, but the flow rates are not consistent
196   for each altitude and filter type, varying up to a factor two for each filter type/line/altitude/campaign.
197   The filter type effect on flow rate can be seen in Fig. 4, where the average flow rate for 0.4 μm
198   polycarbonate filters is about twice the flow rate of the 0.45 μm PTFE filters. In order to investigate
199   the inconsistency in the flow rate at each altitude, we analysed the flow rate data by comparing it with
200   different parameters (ambient air and cabin temperature, ambient air and cabin pressure, wind
201   direction and speed with respect to the aircraft movement), but there was no correlation with any of
202   these variables. Different mesh supports were used, but this does not affect the flow rate significantly
203   according to some ground based tests. We checked the flow rate through each sampling period and
204   found it did not change over time on a particular filter set (even after stopping the sampling and
205   starting it again). In addition, we performed some tests on the ground and during flights to study the
206   effect of potential leaks by inserting paper disks of the same dimension as the filters in the filter
207   holders and found no evidence of leaks in the system.

208 We conclude that this variability in the flow rate comes from variability in the pump performance in
209 combination with subtle differences in individual filter pairs. The side displacement pump is not the
210 ideal pump for this system and operates at its maximum capacity. Hence, we suggest that to improve
211 the performance of the system that flow rates are actively controlled and also the side displacement
212 pump is replaced with a more appropriate design. This would also have the advantage that flow rates
213 would be maintained at smaller pressure drops and allow sampling at higher altitudes.

214

215 **3. FAAM underwing optical particle counters**

216 Later in the paper we compare results from the underwing optical particle counters with our electron
217 microspore derived size distributions, hence we describe the optical instruments here. The BAe-146
218 FAAM research aircraft operates underwing optical particle counters to measure aerosol size
219 distributions. These include the Passive Cavity Aerosol Spectrometer Probe 100-X (PCASP) and the
220 Cloud Droplet Probe (CDP). The PCASP measures particles with diameters in the approximate range
221 0.1-3 μm and the CDP measures the particles with diameters in the range of 2-50 μm. These
222 instruments are placed outside the aircraft fuselage, below the wings. These instruments and the
223 methods for calibration are described in (Rosenberg et al., 2012).

224 The instruments were calibrated and had optical property corrections applied as per Rosenberg et al.
225 (2012). We used a refractive index of $1.56 + 0i$ and a spherical approximation (Mie theory) in the
226 optical property corrections. In Fig. 5, one can see a sensitivity test on the refractive index value we
227 used in order to examine how variability in refractive index affect the bin centres position, their width,
228 and therefore the size distribution obtained from the PCASP and CDP. As one can see in Fig. 5a,
229 modification of the real part of the refractive index from 1.5 to 1.7 can change the position of the
230 PCASP bin centres up to a factor 1.5, but its effect on the CDP is not significant. When varying the
231 imaginary part of the refractive index from 0 to 0.01, the bin centre positions of the first half of the
232 range of the PCASP and CDP do not change but it can change the position of the bins of the end of the
233 range of both instruments (less than a factor 1.5). However, for the purposes of this work, the
234 differences produced by the variation in the refractive index are not large enough to modify the
235 conclusions of the analysis, therefore we use a value of $1.56 + 0i$.

236 The chosen refractive index range for this sensitivity analysis can be justified on the basis that the SEM
237 compositional analysis showed that the composition of the aerosol samples used in this study was
238 very heterogeneous, dominated by carbonaceous particles (biogenic, organic and black carbon) and
239 with some contributions of mineral dust and other particle types. Values of the real part of the
240 refractive index in the 1.5 to 1.6 range are compatible with sodium chloride and ammonium sulphate
241 (Seinfeld and Pandis, 2006), as well as most mineral dusts (McConnell et al., 2010). The range is very
242 close to values for the real part of the refractive index of organic carbon but below the values for black
243 carbon (Kim et al., 2015). As a consequence, the refractive index choice might not be accurate for a
244 black carbon dominated sample. However, black carbon is not likely to dominate in the size range
245 where a value of the real part of the refractive index of 1.7 dramatically changes the size distribution
246 (diameters above 0.5 μm) (Seinfeld and Pandis, 2006), so our refractive index choice is valid. In Fig.
247 5b one can see that changing the imaginary part of the refractive index from 0 to 0.01 only produces
248 small changes in the distribution. The imaginary part of the refractive index of many aerosol types as
249 sodium chloride, sulphates and mineral dust falls within the shown range (Seinfeld and Pandis, 2006),
250 (McConnell et al., 2010). For values of the imaginary part of the refractive index above 0.01 (not shown
251 in the image), the size distribution dramatically changes for sizes above 1 μm (but not for smaller
252 values of it), overlapping and disagreeing with the CDP. However, values above 0.01 in the imaginary

253   part of the refractive index can only happen in black carbon, which will dominate only in the submicron

254   sizes (Seinfeld and Pandis, 2006). The submicron part of the size distribution doesn't change for values

255   of the imaginary part of the refractive index above 0.01, so our refractive index choice is still

256   acceptable even for samples with significant contributions from black carbon in submicron sizes.

257   For the PCASP-CDP, we have considered two uncertainty sources. The first one is the Poisson counting

258   uncertainty in the number of particles in each bin and the second one is the uncertainty in the bin

259   width that is given by the applied optical property corrections. Both sources have been propagated in

260   order to obtain the errors of $dN/d\log D_p$ and $dA/d\log D_p$. Other uncertainties such as the refractive

261   index assumption or particle shape effect, as well as the uncertainty in the bin position haven't been

262   shown in this study. Sampling biases haven't been quantified or corrected yet so they haven't been

263   included. The size distributions produced by the PCASP-CDP have been taken as a reference value for

264   the purposes of this study.

265

266   **4. Scanning Electron Microscopy technique for aerosol characterization**

267   Scanning Electron Microscopy is used in order to study composition and morphology of aerosol

268   particles, in a similar way to previous works such as Chou et al. (2008), Young et al. (2016) and Price

269   et al. (2018). We use a Tescan VEGA3 XM scanning electron microscope (SEM) fitted with an X-max

270   150 SDD Energy-Dispersive X-ray Spectroscopy (EDS) system controlled by an Aztec 3.3 software by

271   Oxford Instruments, at the Leeds Electron Microscopy and Spectroscopy Centre (LEMAS) at the

272   University of Leeds. In order to get data from thousands of particles in an efficient way, data collection

273   was controlled by the AztecFeature software expansion.

274   Aerosol particles were collected with the filter inlet of the FAAM aircraft on polycarbonate track

275   etched filters with 0.4 μm pores (Whatman, Nucleopore). Samples for SEM are usually coated with

276   conductive materials in order to prevent the accumulation of charging on the sample surface (Egerton,

277   2005). For aerosol studies, materials like gold (Hand et al., 2010), platinum (Chou et al., 2008), or

278   evaporated carbon (Krejci et al., 2005; Reid et al., 2003; Young et al., 2016) have been used. When it

279   comes to choosing which signal to detect, some previous studies used backscattered electrons (Gao

280   et al., 2007; Price et al., 2018; Reid et al., 2003; Young et al., 2016) and some others choose secondary

281   electrons (Kandler et al., 2007; Kandler et al., 2011; Krejci et al., 2005). We started the development

282   of this analysis using a carbon coating and the backscattered electron detector. This technique

283   produced reproducible images and almost no artefacts from the pore edges, consistent with Gao et

284   al. (2007). However, we noticed that we were undercounting a significant fraction of the small carbon

285   based particles, which looked transparent under the backscattered electron imaging but not under

286   the secondary electron detector, as seen in Fig. 6. This likely happened because the contrast in the

287   secondary electron images mainly depends on the topography of the sample whereas the contrast in

288   the backscattered electron images depends on the mean atomic number of each sample phase

289   (Egerton, 2005). Since the polycarbonate filters are made of C and O, particles containing only these

290   elements in a similar proportion to the background did not exhibit a high contrast under the

291   backscattered electron detector (Laskin and Cowin, 2001). However, when using secondary electron

292   imaging with carbon coatings, images were less reproducible and contained artefacts from the pore

293   edges, probably resulting from charging or topographical effects. We found that coating the samples

294   with 30 nm of iridium helps to improve the secondary electron image reproducibility and reduced the

295   pore edge artefacts as well as allowing us to locate small organic particles. An increase in the size of

296   the particle as a consequence of the coating may introduce an uncertainty in the size of the smallest

297   particles. An additional advantage of using Ir is that the energy dispersive X-ray spectrum of Ir does
298   not overlap greatly with the elements of interest.

299   In the SEM the sample was positioned at a working distance of 15 mm. The SEM's electron beam had
300   an accelerating voltage of 20 KeV and a spot size chosen to produce the optimum number of input
301   counts in the EDS detector. Images are taken at two different magnifications with a pixel dwell time
302   of 10 μs and a resolution of 1024 x 960 pixels per image. High magnification images (x 5000 or similar)
303   were used to identify particles down to 0.3 or 0.2 μm depending on the sample, and medium
304   magnification images (x1500 or similar) are used to identify particles down to 1 μm. A brightness
305   threshold with upper and lower limits that correspond to pixels of certain shades of grey was manually
306   adjusted for each image by the operator to discriminate particles from the background. Based on the
307   manually set brightness threshold, AztecFeature identified the pixels that fall within the limits as
308   aerosol particles and calculated several morphological properties of the particle as cross sectional
309   area, length, perimeter, aspect ratio, shape factor or equivalent circular diameter. The equivalent
310   circular diameter is defined as $\sqrt{(4\,A\,\pi^{-1})}$, where A the cross sectional area of the aerosol particle.

311   For this analysis we placed a section of the 47 mm filter on a 25 mm stub. In order to collect
312   morphological and chemical information from a few thousand particles, we only scanned a fraction of
313   the filter. We collected information from 5 to 20 different areas, and each area consisted of a montage
314   of several SEM images. The areas were chosen by the user from all over the surface of the selected
315   fraction of the filter, since aerosol particles were evenly distributed all over the central ~30mm of the
316   filter (the area which exposed to the air) as one can see in Fig. 7. Each area was selected in the
317   software, manually adjusting the particle detection threshold. The Z position of the stage was also
318   adjusted manually for each image in order to produce properly focused images. After doing this, the
319   image scanning and EDS acquisition was performed in an automated way. Morphological information
320   was recorded for all particles with an ECD greater than the specified size threshold (typically 0.2 or 0.3
321   μm).

322   EDS analysis was restricted to the first 12 or 15 particles detected in each image. This reduces the
323   likelihood of charging problems caused by exposure to the electron beam. The software performed
324   EDS in the centre of the particles, obtaining around 50,000 counts per particle. The raw data for any
325   given particle were matrix corrected and normalised by the AZtec software to produce element weight
326   percent values with a sum total of 100%, using a value of the confidence interval of 2 (a further
327   discussion on the confidence interval can be seen in Fig. S1). Then particles were categorised based
328   on their chemical composition using a classification scheme which can be created and modified within
329   the AztecFeature software. The characteristic X-rays taken at one point are emitted by a certain
330   interaction volume which is bigger than some of the analysed particles (typically < 2μm³, decreasing
331   with atomic number and increasing with incident electron energy). As a consequence, a part of the X-
332   ray counts attributed to each particle come from the background (C and O from the polycarbonate
333   filter and Ir from the coating) and the weight percentages obtained from the X-ray spectra do not
334   match the actual weight percentages of the particle itself. As a consequence, when categorising the
335   particles based on their composition, we only use the presence or absence of certain elements, and
336   the ratio between the weight percentages of non-background elements. The classification scheme
337   works by checking if the composition of each particle falls within a range of values which are manually
338   defined by the user. Particles not matching the first set of rules are tested again for a second set of
339   rules, and so on, until reaching the last set of rules. A few sets of rules can be merged into a category.
340   In the supplementary information (Fig. S3), we give the details of the 32 sets of rules used, which are
341   then summarised into 10 composition categories. A description of the most abundant elements in
342   each category and an interpretation of these categories is included in Sect. 5.

Atmospheric
Measurement
Techniques
Discussions

343 The detection of particles has certain limitations. The edges of the pores can look brighter than the
344 rest of the filter in the SE images (probably because they consist of a larger surface area from which
345 secondary electrons can be generated, hence a larger signal). As a consequence, they can look like
346 ~0.2 μm particles, which is the main reason why particles below 0.3-0.2 μm (depending on the sample)
347 are not included in this analysis. These artefacts had a chemical composition similar to the filter, so
348 they were labelled as "Carbonaceous" by the classification scheme, falling at the same category as
349 most biogenic and black carbon particles. However, these artefacts were only around 1 to 10 percent
350 depending on the sample. If they appear in larger quantities, they can be removed manually after or
351 during the analysis. Another limitation arises from the fact that some aerosol particles did not have
352 sufficient brightness in the SE image and were not detected as a particle. This happens more
353 frequently for smaller particles, but it can also happen with some larger particles, particularly if they
354 are only composed of Na and Cl or S. This issue can be addressed if necessary by setting a very low
355 limit of detection, which adds lots of artefacts as well as the low brightness particles, and then
356 removing the artefacts manually (the artefacts can be easily identified by the user). In other infrequent
357 instances, only a fraction of the particle had a brightness above the threshold, so they were detected
358 as a smaller particle or multiple smaller particles, or if two particles are close enough, they can be
359 detected as a single larger particle. However, we feel that in the vast majority of the cases a
360 representative cross sectional area of the particle was picked by the software.

361 Blank polycarbonate filters can contain some particles on them from manufacturing or transport
362 before being exposed to the air. In addition, handling and preparing the filters can introduce additional
363 particles to it. In order to assess these artefacts, we scanned a few clean blank filters. We also
364 examined a filter that had been brought to the flight, loaded in the inlet system (but not exposed to a
365 flow of air), and then stored at -18 °C for a few months (like most of the aerosol samples on filters).
366 The results of both the handling blank and the blank can be seen in Fig. S2. The number of particles is
367 very low, typically about the order of magnitude of one particle per 100 by 100 μm square, which is
368 well below the typical particle loading on a filter exposed to the atmosphere. In Fig. S2 one can see
369 that the vast majority of particles found in both blank filters and the handling blank belong to the
370 metallic rich category. However, further examination of the composition of these particles revealed
371 that almost all of them were Cr rich particles (about 97 % in the case of the blank filters and about
372 96% in the case of the handling blank). As a consequence, we excluded all the Cr rich particles from
373 the analysis of atmospheric aerosol (it was only ever a very minor component). By doing this, we make
374 sure that we excluded more than half of the artefacts of the analysis. The composition of the particles
375 present in the blank filters and in the handling blank was very similar, suggesting that most of these
376 artefacts are not produced by the loading, manipulation and storage of the filter. However, there was
377 a very small but significant contribution of mineral dust origin particles (Al-Si rich, SI rich and Si only)
378 for sizes in between 0.7 and 5 μm in the handling blank, which should be taken into consideration.

379

380 5. Inlet characterisation and sampling efficiency using Scanning Electron Microscopy

381 In order to experimentally test the inlet efficiency, to complement the efficiency calculations
382 presented in Section 2.2, we have used SEM to quantify the size distribution of particles collected on
383 filters (Sect. 4) and compare this with the measurements from the under-wing optical probes (Sect.
384 3). The calculations in Sect. 2.2 suggest that there is an enhancement of the coarse mode aerosol
385 particles, which is larger when sampling with the bypass closed. To test this we have collected aerosol
386 onto 0.4 μm pore size polycarbonate filter in both lines in parallel. In one of the lines, the bypass was
387 kept open, and in other line the bypass was kept closed. Using our SEM approach described in the
388 Sect. 4, we calculated the size distribution of the aerosol particles on top of each filter. We compared

389 these size distributions with the ones measured by the underwing optical probes (PCASP-CDP), as
390 described in Sect. 3. We performed the test twice in two different test flights based in the UK.

391 The results of these comparisons can be seen in Fig. 8 and Fig. 9 for both number and surface area size
392 distribution. There are some discrepancies between the optical probes and the SEM size distributions
393 from the filters, which has also been reported in previous works (Chou et al., 2008), (Price et al., 2018;
394 Young et al., 2016). There is significant disagreement between the submicron particles detected on
395 top of the filter and the submicron particles detected in situ by the PCASP-CDP in Fig. 9a in a very
396 similar way to Young et al. (2016). Since the 0.4 µm polycarbonate filters have a high collection
397 efficiency at these length scales (Lindsley, 2016; Soo et al., 2016), the disagreement at the submicron
398 regime could be produced by several effects. Some small particles that may not have sufficient
399 brightness to be detected might produce some undercounting, despite the fact we made efforts to
400 mitigate this problem. Also, volatilization of certain type of aerosol particles (which are more abundant
401 in the submicron fraction (Seinfeld and Pandis, 2006)) can happen during heating or sampling (Bergin
402 et al., 1997; Hyuk Kim, 2015; Nessler et al., 2003) and this effect could be enhanced by the fact that
403 samples are exposed to high vacuum during the SEM analysis. The presence of nitrates could be tested
404 using an aerosol mass spectrometer. In addition, the SEM techniques measure the dry diameter and
405 the optical probes measure the aerosol diameter at ambient humidity. This hygroscopic effect is
406 known to shift the dry size distributions to smaller sizes, which could also explain part of the
407 disagreement (Nessler et al., 2003; Young et al., 2016). Disagreement in the measurements can be
408 also produced by the fact that the techniques are measuring different diameters; optical diameter in
409 the case of the PCASP-CDP and circular equivalent geometric diameter in the case of the SEM.

410 One can see that the concentration of aerosol particles measured by the SEM on the filters was higher
411 than the particles detected by the optical probes for sizes above ~8 µm in Fig. 8 and Fig. 9. These
412 results are consistent with Price et al. (2018), where they observed a similar enhancement of large
413 aerosol particles in two mineral dust dominated samples collected close to Cape Verde. In addition,
414 the enhancement was larger when sampling under closed bypass conditions. The results of these
415 comparisons are in agreement with the theoretical calculations in Sect. 2.2.

416 In Fig. 10 we have presented some other SEM size distributions compared with the PCASP-CDP data
417 from three different aerosol samples in contrasting locations. Since these data were taken during the
418 scientific field campaigns and not test flights, we only collected one polycarbonate filter for SEM since
419 the other line was used for INPs analysis on Teflon filters. All the sampling was done with the bypass
420 open. The agreement between the optical and SEM obtained size distributions in Fig. 10 is similar to
421 the one in Fig. 8 and Fig. 9 (for the open bypass case). One can observe in Fig. 10c that there was a
422 loss of particles smaller than ~0.5 µm and also that in Fig. 10a and Fig. 10b there was an enhancement
423 of the coarse mode.

424 The data shown in this section have been obtained in very different locations (South England in the
425 case of Fig. 8, Fig. 9 and Fig. 10a, Iceland in the case of Fig. 10b and north Alaska in the case of Fig. 10c.
426 As a consequence, the studied aerosol samples are very different in both morphology and chemistry.
427 From the comparisons, we can state that the sampling carried out by the filter system has certain
428 biases, but it captures particles with a size distribution with similar features to the ones measured by
429 the underwing optical probes.

430

Atmospheric
Measurement
Techniques
Discussions

6. Recommendations for aerosol sampling with the Filters system on the FAAM aircraft

Based on the calculations in Sect. 2.1, we suggest keeping the total flow rate (including the flow through the filters measured by the electronics box plus the bypass flow, which can be between 20 and 35 L min^{-1}) above 50 L min^{-1}. Below this range, the sub-isokinetic enhancement of large aerosol particles is above a factor 2, according to the calculations in Sect. 2.2 that can be seen in Fig. 2b. For total flow rates above 65 L min^{-1}, the flow becomes turbulent throughout the line, which associated losses. However, the calculations shown in Fig. 2c indicate that the combination of the isokinetic enhancements and turbulent losses at 80 L min^{-1} lead to a reasonably representative sampling, but when it reaches 150 L min^{-1}, the position of the D50 drops to 6.5 μm (not shown in the graph) so such a high flow rate would not be ideal if the user wants to sample coarse aerosol particles. Hence, we recommend an operational upper limit of 80 L min^{-1}. For 0.45 μm PTFE filters and the 0.4 μm polycarbonate filters presented in Fig. 4, sampling close to this flow rate range is often achievable by keeping the bypass open, since this increases the total flow rate and brings it closer to the suggested range, as one can see in Fig. 2c. If other filter types are used, these results should be taken in consideration when choosing the pore size or equivalent pore size in order to avoid dramatic sampling biases.

We already mentioned in Sect. 2.3 that we recommend replacing the side displacement pump with a design that would provide a greater pressure drop. In addition, we also recommend that the bypass flow rate is also routinely measured and controlled in order that the flow at the inlet nozzle can be optimised while sampling.

7. SEM compositional categories

Here we describe the 10 categories we have used in our compositional analysis, which are a summary of the 32 rules described in the supplementary information. The approach has some similarities with the ones in previous studies (Chou et al., 2008; Hand et al., 2010; Kandler et al., 2011; Krejci et al., 2005; Young et al., 2016), but it is distinct. Because of the fact that the filter is made of C and O, background elements (C and O) were detected in all the particles. Particles in each category can contain smaller amounts of other elements apart from the specified ones. This classification scheme has been designed a posteriori to categorise the vast majority of the aerosol particles in the three field campaigns previously described and some ground collected samples in the UK and Barbados. The main limitation of the classification scheme is the difficulty to categorise internally mixed particles. The algorithm has been built in a way it can identify mixtures of mineral dust and sodium chloride (they appear as mineral dust but they could be split into a different category if necessary) and sulphate or nitrate ageing on sodium chloride (they appear as Na rich but it could also be split into a different category). However, other mixtures of aerosol wouldn't be identified, and they would be categorised by the main component in the internal mixture in most cases.

7.1. Carbonaceous

The particles in this category contained only background elements (C and O). The components of the carbonaceous particles consist in either black carbon from combustion processes or organic material, which can be either directly emitted from sources or produced by atmospheric reactions (Seinfeld and Pandis, 2006). Particles containing certain amount of K and P in addition to the background elements were also accepted in these category. These elements are consistent with biogenic origin aerosol particles (Artaxo and Hansson, 1995). Distinction between organic and black carbon aerosol unfortunately could not reliably be done. Since N is not analysed in our SEM set up, any nitrate aerosol particle would fall into this category if it is on the filter. However, since these particles are semi-

Atmospheric
Measurement
Techniques
Discussions

Open Access

475 volatile, some of these aerosol particles would not resist the low pressure of the SEM chamber. This
476 could be further investigated in the future.

477 7.2. S rich

478 Aerosol particles in this category contained a substantial amount of S. These EDS signals are
479 compatible with sulphate aerosol particles, which are solid or liquid sulphuric acid particles (Kumar
480 and Francisco, 2017). In the same way as the nitrates, this particles are semi-volatile and some of them
481 might not resist the low pressure of the SEM chamber.

482 7.3 Metal rich

483 The composition of particles in this category is dominated by one of the following metals: Fe, Cu, Pb,
484 Al, Ti, Zn or Mn. These EDS signatures are compatible with metallic oxides or other metal rich particles.
485 These metal containing particles can originate from both natural sources and anthropogenic sources.
486 Some metallic oxides are common crustal materials that could go into the atmosphere but are also
487 produced during some combustion processes (Seinfeld and Pandis, 2006). In addition, many types of
488 metal and metallic derivatives particles are produced as component of industrial emissions and other
489 anthropogenic activities (Buckle et al., 1986), (Fomba et al., 2015).

490 7.4. Na rich

491 Sodium chloride particles are the main component of the sea spray aerosol particles which are emitted
492 through wave breaking processes (Cochran et al., 2017). These particles can age in the atmosphere by
493 reacting with atmospheric components such as sulphuric or nitric acid (Graedel and Keene, 1995),
494 (Seinfeld and Pandis, 2006). As a consequence of this reaction, a part of their Cl content will end up in
495 the gaseous phase (as HCl), leading to an apparent chlorine deficit in the aged sea spray aerosol
496 particles. Particles in this category have an EDS signature compatible with sea spray aerosol particles
497 since they are identified by the presence of Na, containing in most cases Cl and/or S (N is not included
498 in our SEM analysis).

499 7.5 Cl rich

500 Particles in this category contained mainly Cl and sometimes also K but never Na, so they are not
501 sodium chlorine particles. Significant concentrations of Cl and metals in aerosol particles have been
502 linked to industrial activities and automobile emissions (Paciga et al., 1975), whereas Cl and K in
503 aerosol particles could be originated by the use of fertilisers (Angyal et al., 2010), or emitted during
504 pyrotechnic events (Crespo et al., 2012).

505 7.6 Ca rich

506 The composition of the particles in this category is dominated by Ca. In this category, particles
507 containing only Ca (plus C and O, the background elements) are consistent with calcium carbonate, a
508 major component of mineral dust (Gibson et al., 2006). If other elements such as Mg and S are present,
509 the signature of the particles compatible with some mineral origin elements as gypsum and dolomite
510 respectively. In addition, presence of minor amounts of Si, Al and other elements could indicate mixing
511 of these Ca rich particles with some other soil components as silicates. However, since Ca is a biogenic
512 element, we cannot discard the biogenic origin of some of the Ca-rich particles (Krejci et al., 2005).

513 7.7 Al-Si rich

514 Particles in the Al-Si rich category were detected by the presence of Al and Si as major elements. Very
515 often, this particles also contained smaller amounts of Na, Mg, K, Ca, Ti, Mn and Fe. Particles in this

516   category are very likely to have mineral origin and are commonly described as aluminosilicates which
517   include a range of silicates such as feldspars and clays (Chou et al., 2008; Hand et al., 2010). Mixed
518   mineral origin particles containing both Al and Si can also fall into this category. Strong presence of Na
519   and Cl could indicate internal mixing with some sea spray aerosol, whereas a strong S presence could
520   indicate atmospheric acid ageing.

521   7.8 Si only

522   The particles in this category contained only Si apart from the background elements. Particles in this
523   category are very likely to be a silica polymorph (mainly quartz), one of the major components of the
524   earth's crust. Since we cannot determine if the C signal in the EDS of these particles is produced from
525   the background or from the particle itself, a particle containing only C, Si and O would fall into this
526   category, however, mineral phases containing these elements are extremely rare.

527   7.9 Si rich

528   The composition of these particles was dominated by Si, and other elements Na, Mg, K, Ca, Ti, Mn and
529   Fe. The main difference with the particles in Sect. 7.7 is that the ones described here didn't contain Al
530   above the limit of detection. The EDS signal of particles in this category is compatible with any silicate
531   that does not contain Al as a major component in its phase such as talc or olivine. The only exception
532   is quartz, which falls in the 'Si only' category described above. They could also be internal mixtures of
533   silica or silicates without aluminium as a major component in its phase. Because of the high limit of
534   detection of the Al (See the SI), some particles in this category could contain small amounts of Al, and
535   should belong to Al-Si rich category. As in the Al-Si rich particles case, strong presence of Na and Cl
536   could indicate internal mixing with some sea spray aerosol, whereas a strong S presence could indicate
537   atmospheric acid ageing.

538   Some of these categories could be further grouped. For example, the particles in the Ca rich, Al-Si
539   rich, Si only and Si rich categories could be considered as "mineral dust". However, if the sample
540   contains ash from combustion processes or volcanic origin, it will also appear in these last categories
541   since its composition is similar to mineral dust (Chen et al., 2012; Nakagawa and Ohba, 2003).

542   **8. Application to a sample collected from the atmosphere above S.E. England**

543   The SEM technique described in Sect. 4 has been applied to samples collected from the FAAM aircraft
544   in various locations. Here we show an example of some of the capabilities of the developed technique
545   applied to one of the samples collected in S. E. England; the resulting size resolved composition is
546   shown in Fig. 11. The fraction of particles corresponding to each compositional category described in
547   Sect. 7 for each size can be seen in Fig. 11a. The SEM size distribution of each composition category
548   can be seen in Fig. 11b. By looking at this analysis, one can see that the sample was clearly dominated
549   by carbonaceous aerosol particles in all the sizes, but there was a clear mineral dust mode (Si only, Si
550   rich Al-Si rich and Ca rich) and some smaller contributions of other aerosol types (metal rich and S
551   rich). A potentially useful application of the size resolved composition is calculating the surface area
552   or mass of an individual component of a heterogeneous aerosol. As an example, we have grouped the
553   mineral dust categories Si only, Si rich Al-Si rich and Ca rich to produce the surface area size
554   distribution of mineral dust (and potentially ash) in Fig. 11c.

555   There are very few ways to obtain the size-resolved composition of an aerosol sample. Single particle
556   laser based mass spectroscopy has been used in order to obtain the size-resolved composition of
557   aerosol samples, both on the ground and in an aircraft (Pratt and Prather, 2012), (Wendisch and
558   Brenguier, 2013). Examples of this are instruments like the Particle Analysis by Laser Mass

559 Spectrometer (PALMS) (Cziczo et al., 2006; Thomson et al., 2000), the Aerosol Time-Of-Flight Mass
560 Spectrometer (ATOFMS) (Pratt et al., 2009), or the Aircraft-Based Laser Ablation Aerosol Mass
561 Spectrometer (ALABAMA) (Brands et al., 2011). However, a limitation of these techniques is that they
562 focus on the fine mode, with limited information about the coarse mode. A size-resolved
563 compositional analysis as the one described here is able to obtain the accumulation and coarse mode
564 size distribution of mineral dust in most aerosol samples, even in the ones dominated by other species,
565 as shown in Fig. 11. In addition, this approach can be used to get size-dependent information about
566 the shape factor and other morphological properties of the mineral dust, as well as ratios in between
567 the element concentrations.

568 **9. Conclusions**

569 In this work we have characterised the filter inlet system on board the BAe-146 UK FAAM research
570 aircraft which is used for the collection of atmospheric aerosol particles for off line analysis. Our
571 primary goal is to use this inlet system for quantification of INP concentrations and size resolved
572 composition measurements, but it could also be used to derive other quantities with other analytical
573 techniques.

574 In order to characterise the inlet system we made use of an electron microscope technique to study
575 the inlet efficiency, by comparing the SEM size distributions with the in situ size distributions
576 measured with underwing optical probes (PCASP-CDP). The sub-isokinetic enhancement of large
577 aerosol particles predicted by the calculations in Sect. 2.2 was observed in these comparisons. We also
578 experimentally verify that this enhancement is minimised by operating the inlet with the bypass open
579 which maximised the flow rate through the inlet nozzle. In addition, we note that we performed tests
580 with three very different aerosol distributions and the size distribution of the particles on the filters
581 was comparable to those measured by the underwing optical probes. Overall, the inlet tends to
582 enhance the concentration of aerosol in the coarse mode with a peak enhancement at ~10 μm. The
583 inlet efficiency decreases rapidly for sizes above about 20 μm and becomes highly dependent upon
584 the specifics of the sampling such as flow rates and angle of attack. Based on these tests we
585 recommend that the total flow rates at the nozzle are maintained at between 50 and 80 l min^{-1}, and
586 also that improvements are made to the pump and bypass flow control (see Sect. 2.3).

587 We also established an SEM technique to determine the size resolved composition of the aerosol
588 sample. Each particle can be categorized based on its chemical composition using a custom made
589 classification scheme. Using this technique we showed that the filter system on board of the BAe-146
590 spreads the particles evenly across the filter surface, which is necessary for the SEM size distribution
591 analysis.

592 Having a well characterised inlet allows us to sample aerosol particles up to around 20 μm with
593 knowledge of the likely biases from the aircraft. Hence, we can use this inlet system to collect aerosol
594 for offline analysis at altitudes which are relevant for clouds. For example, this may allow us to use the
595 size resolved aerosol composition to quantify the size distribution of individual aerosol components
596 at a particular location and combine this information with INP measurements to quantify the surface
597 area normalised ice nucleating ability of a specific class of aerosol.

598

599 **Appendix A: discussion of the inlet efficiency calculations**

600 Here we include a further description of the efficiency mechanisms used in the inlet model described
601 in Fig. 2 and discuss the choice of the equations and their limits of validity:

602 *Aspiration efficiency* accounts for the fact that the speed of the sampled air mass (U_0), and the speed
603 of the air through the beginning of the nozzle (U) are different. When these two speeds are equal, the
604 sampling is called "isokinetic", whereas when the speeds don't match, the sampling is called super
605 isokinetic or sub-isokinetic depending on if U_0 is smaller or larger than U respectively. In our case, the
606 air mass moves at the flying speed, which varies with the altitude (110 m s^{-1} is a typical value for
607 sampling altitudes), and the speed at the start of the inlet is almost always below 35 m s^{-1} (sub-
608 isokinetic conditions). As a consequence, some air streamlines will be forced around the inlet, while
609 high inertia particles won't, which will lead to an aspiration efficiency above 1 for coarse mode aerosol
610 particles. This enhancement is greater for large particles due to their large inertia which makes difficult
611 their ability to follow the air streamlines. The enhancement reaches a maximum value of U_0/U in its
612 high diameter limit (when none of the particles in the sampled air mass follow the streamlines that
613 escape from the inlet and all of them are sampled). The aspiration efficiency tends to 1 (no
614 enhancement) for small diameters.

615 This behaviour has been characterised by several studies (we will only look at the sub-isokinetic range
616 of the equations since it is impossible to reach the super isokinetic range during flight). An empirical
617 equation was developed based on laboratory experiment by Belyaev and Levin (1972) and Belyaev
618 and Levin (1974) (referred as B&L) for certain range of U/U_0 ratio and Stokes number. However, for
619 ratios below its experimental range ($U/U_0 > 0.2$), the B&L function doesn't make physical sense since
620 it converges to values above 1 for small particle sizes. The aircraft inlet system works at smaller U/U_0
621 ratios sometimes, so this function is not very accurate to describe the behaviour of the system in such
622 conditions. Liu et al. (1989) developed another function (referred as LZK) by means of a numerical
623 simulation based on computational fluid mechanics. The U/U_0 ratio and Stokes number valid range is
624 wider than the B&L expression (down to 0.1). It agrees with the B&L expression in the U/U_0 ratio the
625 latter was developed for. For smaller values of the ratio, the LZK function are believed to be more
626 accurate, since it predicts the known physical behaviour (no sub-isokinetic enhancement for small
627 particle sizes). It reaches U/U_0 ratios down to 0.2, which is enough to cover most of the total flow
628 rates achieved in the inlet system. (Krämer and Afchine, 2004) developed another expression (referred
629 as K&A) for $0.007 < U/U_0 < 0.2$ based on computational fluid dynamics. However, for low particle sizes,
630 the efficiency doesn't converge to 1. As a consequence, we have used the LZK (Liu et al., 1989) function
631 since it covers most of the U/U_0 ratios we get in the inlet system, it agrees with the experimental data
632 in Belyaev and Levin (1972) and Belyaev and Levin (1974) and it converges to U_0/U for large particles
633 sizes and 1 for small particle sizes. Outside its valid range ($U/U_0 < 0.1$), the LZK function agrees with
634 the K&A function for large radius and converges to 1 for small particle sizes. The equation is valid for
635 $0.01 < Stks < 100$, which is enough to cover the range in between 1 and 100 µm. As already stated, it
636 tends to 1 for small particles sizes and to U_0/U for large particles sizes (At 50 L min^{-1}, the ratio U/U_0 is
637 0.2). All the calculations were done under standard conditions (0 $^\circ$C and 1 bar).

638 *Inlet inertial deposition i*s defined as the inertial loss of aerosol particles when they enter nozzle. It is
639 produced by the fact that the streamlines bend towards the walls at the moment they enter the
640 nozzle, some large inertia particles can impact the walls and get deposited. Here, we have used the
641 equation given in Liu et al. (1989) which quantifies this effect. It is also valid for $0.01 < Stks < 100$, which
642 is enough to cover the range in between 1 and 100 µm.

Atmospheric
Measurement
Techniques
Discussions

643   *Turbulent inertial deposition* happens when some particles are collected by the wall when travelling
644   in a pipe in the turbulent regime because some of the particles cannot follow the eddies of the
645   turbulent flow. In order to include this mechanism, we used the equation given in Brockmann (2011),
646   using the relation in between the deposition velocity and dimensionless particle relaxation time given
647   by Liu and Ilori (1974). These calculations are valid for a cylindrical pipe, whereas the turbulent section
648   of the inlet considered here is the nozzle, which has a conical shape. In order to account for this, we
649   divided the conical nozzle into 90 conical sections with an increasing diameter and a length of 1mm,
650   and combined the effect of all the sections. As already mentioned, above 65 L min^{-1}, turbulent flow
651   occurs in the whole inlet tube. This has been taken into account in the 80 L min^{-1} case in Fig. 2b. The
652   equation used here has been tested for size ranges in between 1.4 and 20 µm, and doesn't depend on
653   the Reynolds number values it was tested for (10000 and 50000) (Liu and Ilori, 1974).

654   *Bending inertial deposition* was also considered, since the line curves with an angle of 45° in order to
655   bring the airstream into the cabin. The inertia of some particles may keep them in their original track
656   and they are not able to follow the air streamlines that are bending towards the cabin, following the
657   inlet tubes. In order to account for these losses, we have used the empirical equation given in
658   Brockmann (2011) based on the data from Pui et al. (1987) for laminar flow. This equation was
659   developed for Reynold numbers of 1000, and we have used it for higher values. However, in
660   Brockmann (2011), one can see that the data from Pui et al. (1987) for Re=6000 (beginning of the
661   turbulent flow regime) doesn't differ that much from the fit we have used (valid for Re=1000). Since
662   our Re numbers for the thick section of the tube almost never go above 5000, we can still use the
663   laminar flow fit. This model has been tested for 0.08 < Stks < 1.2, which is enough to cover most of the
664   range where the inertial deposition efficiency drops from 1 to 0. The main caveat of this calculation is
665   that the model considers that the flow rate before and after the bending is the same, while in the inlet
666   system, if the bypass flow is on, the flow rate before and after the bending is different (before it, it
667   would be equal to the total flow rate, whereas after the bending, it would be equal to the filter flow
668   rate). As a consequence we assumed that the flow rate after the bending is equal to the total flow
669   rate.

670   *Gravitational settling* was also considered. We used the analytical equation given by Thomas (1958),
671   as stated in Brockmann (2011). We applied this equation for the section of the pipe from the nozzle
672   to the bend (15 cm long). We used the modification (also analytical) of the previous equation given in
673   Heyder and Gebhart (1977) in order to account for the losses in the second section of the tube which
674   is 40 cm long and it is bended 45°. The gravitational losses in the nozzle were neglected since the
675   settling distance is much shorter and the time the air takes to pass it is smaller since it travels quicker.
676   As stated previously, the lower part of the turbulent regime can be reached for high flow rates through
677   all the tube. For these cases, we still use this equation which is only valid for the laminar regime, since
678   the gravitational settling efficiencies for the turbulent regime are very close to the laminar regime
679   ones (Brockmann, 2011) and wouldn't make a significant difference in our calculations.

680   *Diffusional efficiency* accounts for the fact that small aerosol particles could diffuse to the walls of the
681   pipe via Brownian motion. In order to account for this phenomenon, we have used the analytic
682   equation by Gormley and Kennedy (1948) as stated in Brockmann (2011). We have assumed that
683   diffusion happens only in the tube (before and after the bend) and excluding the diffusion in the nozzle
684   since it is negligible because these losses are a function of the residence time and the residence time
685   of the aerosol particles in the nozzle is much smaller than the rest of the tube. F or this calculation,
686   we have assumed 0 °C and 1 atm. We didn't show the efficiency associated to diffusion in Fig. 2a
687   because it was very close to 1 for all considered sizes. It only becomes slightly smaller than 1 for sizes
688   below 20 nm at 50 L min^{-1}. As a consequence, the inlet could be potentially used to sample nucleation

Atmospheric
Measurement
Techniques
Discussions

689   mode aerosol particles, even though for this study we will only focus on the particles larger than 0.1
690   µm.

691   *Filter collection efficiency* accounts for the fact that some particles can pass through the pores of the
692   filter, if they are smaller than the pores. However, filter pore size (in the case of polycarbonate
693   capillarity filters) and filter equivalent pore size (in the case of PTFE porous filters) is sometimes
694   misunderstood as a size cut off at which smaller particles are lost and larger particles are captured.
695   However, particle collection on filters happens through several mechanisms including interception,
696   impaction, diffusion, gravitational settling or by electrostatic attraction under certain conditions
697   (Flagan and Seinfeld, 1988; Lee and Ramamurthi, 1993). As a consequence, particles with diameters
698   below the pore size are normally collected (Lindsley, 2016; Soo et al., 2016). 99.48% of the generated
699   sodium chloride particles with sizes in between 10.4 and 412 nm were collected by a 0.4 µm
700   polycarbonate filter at flow rates below 11.2 L min^{-1} (smaller than most of the flow rates at which the
701   air passes through the same filters in the FAAM filter inlet system) (Soo et al., 2016). As a consequence,
702   we assumed a filter collection efficiency of 100% across the whole considered size range (0.1 to 100
703   µm).

704   *Anisoaxial losses* have not been considered in the analysis shown in Fig. 2, after estimating that they
705   would only affect particles significantly larger than 10 µm and the fact that the alignment of the inlet
706   is difficult to quantify and the angle of attack changes during the flight. Using the equations explained
707   in Hangal and Willeke (1990a), we calculated that the modification of the sub-isokinetic behaviour of
708   the inlet produced by small values of θ is negligible. The equation was used beyond its experimental
709   limit, but this extrapolation was justified by the fact that the equation for θ = 0 made asymptotic
710   physical sense at the low and high Stokes number limits and produced very similar results to the ones
711   showed in Fig. 2a. Anisoaxial sampling can also produce inertial losses when particles impact the walls
712   of the inlet. These ones have been quantified using the expression given by Hangal and Willeke
713   (1990b) for different values of θ and they can be seen in Fig. 3. This mechanism looks very similar to
714   the gravitational and bend deposition efficiency shown in Fig. 2a. Anisoaxial inertial losses add a cut
715   off that prevents large particles to be sampled. As one can see in Fig. 3, the effect is very dependent
716   on the angle and only affects particles significantly larger than 10 µm in most cases, so it hasn't been
717   included in the total analysis shown in the Fig 2. One can see in Fig. 3 that the position of the D50 of
718   the anisoaxial cut off decreases when increasing values of θ up to 2°. For values of θ between 2° and
719   6°, it increases when increasing θ.

720

732

Atmospheric
Measurement
Techniques
Discussions

733 **References**

734 Albrecht, B. A.: Aerosols, cloud microphysics, and fractional cloudiness, Science, 245, 1227-1230, 1989.

735 Andreae, M. O., Berresheim, H., Andreae, T. W., Kritz, M. A., Bates, T. S., and Merrill, J. T.: Vertical-
736 Distribution of Dimethylsulfide, Sulfur-Dioxide, Aerosol Ions, and Radon over the Northeast Pacific-
737 Ocean, J. Atmos. Chem., 6, 149-173, 1988.

738 Andreae, M. O., Elbert, W., Gabriel, R., Johnson, D. W., Osborne, S., and Wood, R.: Soluble ion
739 chemistry of the atmospheric aerosol and SO2 concentrations over the eastern North Atlantic during
740 ACE-2, Tellus B, 52, 1066-1087, 2000.

741 Angyal, A., Kertész, Z., Szikszai, Z., and Szoboszlai, Z.: Study of Cl-containing urban aerosol particles by
742 ion beam analytical methods, Nucl. Instrum. Methods Phys. Res. B, 268, 2211-2215, 2010.

743 Artaxo, P. and Hansson, H. C.: Size Distribution of Biogenic Aerosol-Particles from the Amazon Basin,
744 Atmos. Environ., 29, 393-402, 1995.

745 Baumgardner, D., Brenguier, J. L., Bucholtz, A., Coe, H., DeMott, P., Garrett, T. J., Gayet, J. F., Hermann,
746 M., Heymsfield, A., Korolev, A., Kramer, M., Petzold, A., Strapp, W., Pilewskie, P., Taylor, J., Twohy, C.,
747 Wendisch, M., Bachalo, W., and Chuang, P.: Airborne instruments to measure atmospheric aerosol
748 particles, clouds and radiation: A cook's tour of mature and emerging technology, AtmRe, 102, 10-29,
749 2011.

750 Baumgardner, D. and Huebert, B.: The airborne aerosol inlet workshop: Meeting report, J. Aerosol Sci,
751 24, 835-846, 1993.

752 Belyaev, S. P. and Levin, L. M.: Investigation of aerosol aspiration by photographing particle tracks
753 under flash illumination, J. Aerosol Sci, 3, 127-140, 1972.

754 Belyaev, S. P. and Levin, L. M.: Techniques for collection of representative aerosol samples, J. Aerosol
755 Sci, 5, 325-338, 1974.

756 Bergin, M. H., Ogren, J. A., Schwartz, S. E., and McInnes, L. M.: Evaporation of ammonium nitrate
757 aerosol in a heated nephelometer: Implications for field measurements, Environ. Sci. Technol., 31,
758 2878-2883, 1997.

759 Brands, M., Kamphus, M., Böttger, T., Schneider, J., Drewnick, F., Roth, A., Curtius, J., Voigt, C., Borbon,
760 A., Beekmann, M., Bourdon, A., Perrin, T., and Borrmann, S.: Characterization of a Newly Developed
761 Aircraft-Based Laser Ablation Aerosol Mass Spectrometer (ALABAMA) and First Field Deployment in
762 Urban Pollution Plumes over Paris During MEGAPOLI 2009, Aerosol Sci. Technol., 45, 46-64, 2011.

763 Brockmann, J. E.: Aerosol Transport in Sampling Lines and Inlets. In: Aerosol Measurement, John Wiley
764 & Sons, Inc., 2011.

765 Buckle, R., Tsakiropoulos, P., and C. Pointon, K.: Preparation and properties of metallic aerosol
766 particles, Int. Mater. Rev., 31, 258-288, 1986.

767 Chen, H., Laskin, A., Baltrusaitis, J., Gorski, C. A., Scherer, M. M., and Grassian, V. H.: Coal fly ash as a
768 source of iron in atmospheric dust, Environ. Sci. Technol., 46, 2112-2120, 2012.

769 Chou, C., Formenti, P., Maille, M., Ausset, P., Helas, G., Harrison, M., and Osborne, S.: Size distribution,
770 shape, and composition of mineral dust aerosols collected during the African Monsoon
771 Multidisciplinary Analysis Special Observation Period 0: Dust and Biomass-Burning Experiment field
772 campaign in Niger, January 2006, J. Geophys. Res. Atmos., 113, 1-17, 2008.

773 Cochran, R. E., Ryder, O. S., Grassian, V. H., and Prather, K. A.: Sea Spray Aerosol: The Chemical Link
774 between the Oceans, Atmosphere, and Climate, Acc. Chem. Res., 50, 599-604, 2017.

775 Crespo, J., Yubero, E., Nicolas, J. F., Lucarelli, F., Nava, S., Chiari, M., and Calzolai, G.: High-time
776 resolution and size-segregated elemental composition in high-intensity pyrotechnic exposures, J.
777 Hazard. Mater., 241-242, 82-91, 2012.

778 Cziczo, D. J., Thomson, D. S., Thompson, T. L., DeMott, P. J., and Murphy, D. M.: Particle analysis by
779 laser mass spectrometry (PALMS) studies of ice nuclei and other low number density particles, Int. J.
780 Mass spectrom., 258, 21-29, 2006.

781 DeMott, P. J., Prenni, A. J., Liu, X., Kreidenweis, S. M., Petters, M. D., Twohy, C. H., Richardson, M. S.,
782 Eidhammer, T., and Rogers, D. C.: Predicting global atmospheric ice nuclei distributions and their
783 impacts on climate, Proc Natl Acad Sci U S A, 107, 11217-11222, 2010.

784 Egerton, R. F.: Physical principles of electron microscopy, Springer US, 2005.

785 Flagan, R. C. and Seinfeld, J. H.: Removal of particles from gas streams. In: Fundamentals of Air
786 Pollution Engineering, Prentice-Hall, Inc., Englewood Cliffs, NJ, 1988.

787 Fomba, K. W., van Pinxteren, D., Muller, K., Iinuma, Y., Lee, T., Collett, J. L., and Herrmann, H.: Trace
788 metal characterization of aerosol particles and cloud water during HCCT 2010, Atmos. Chem. Phys, 15,
789 8751-8765, 2015.

790 Gao, Y., Anderson, J. R., and Hua, X.: Dust characteristics over the North Pacific observed through
791 shipboard measurements during the ACE-Asia experiment, Atmos. Environ., 41, 7907-7922, 2007.

792 Gibson, E. R., Hudson, P. K., and Grassian, V. H.: Aerosol chemistry and climate: Laboratory studies of
793 the carbonate component of mineral dust and its reaction products, Geophys Res Lett, 33, 1-5, 2006.

794 Gormley, P. G. and Kennedy, M.: Diffusion from a Stream Flowing through a Cylindrical Tube, Math.
795 Proc. Royal Ir. Acad., 52, 163-169, 1948.

796 Graedel, T. E. and Keene, W. C.: Tropospheric budget of reactive chlorine, Global Biogeochem. Cycles,
797 9, 47-77, 1995.

798 Hand, V. L., Capes, G., Vaughan, D. J., Formenti, P., Haywood, J. M., and Coe, H.: Evidence of internal
799 mixing of African dust and biomass burning particles by individual particle analysis using electron
800 beam techniques, J. Geophys. Res., 115, 1-11, 2010.

801 Hangal, S. and Willeke, K.: Aspiration efficiency: unified model for all forward sampling angles, Environ.
802 Sci. Technol., 24, 688-691, 1990a.

803 Hangal, S. and Willeke, K.: Overall Efficiency of Tubular Inlets Sampling at 0-90 Degrees from Horizontal
804 Aerosol Flows, Atmos Environ a-Gen, 24, 2379-2386, 1990b.

805 Haywood, J. and Boucher, O.: Estimates of the direct and indirect radiative forcing due to tropospheric
806 aerosols: A review, Rev Geophys, 38, 513-543, 2000.

807 Heyder, J. and Gebhart, J.: Gravitational deposition of particles from laminar aerosol flow through
808 inclined circular tubes, J. Aerosol Sci, 8, 289-295, 1977.

809 Hoose, C. and Mohler, O.: Heterogeneous ice nucleation on atmospheric aerosols: a review of results
810 from laboratory experiments, Atmos. Chem. Phys, 12, 9817-9854, 2012.

811 Hyuk Kim, C.: Characterization of Volatilization of Filter-Sampled PM2.5 Semi-Volatile Inorganic Ions
812 Using a Backup Filter and Denuders, Aerosol Air Qual. Res., 2015, 2015.

813 Kandler, K., Benker, N., Bundke, U., Cuevas, E., Ebert, M., Knippertz, P., Rodríguez, S., Schütz, L., and
814 Weinbruch, S.: Chemical composition and complex refractive index of Saharan Mineral Dust at Izaña,
815 Tenerife (Spain) derived by electron microscopy, Atmos. Environ., 41, 8058-8074, 2007.

Atmospheric
Measurement
Techniques
Open Access
Discussions
EGU

816   Kandler, K., Lieke, K., Benker, N., Emmel, C., Kupper, M., Muller-Ebert, D., Ebert, M., Scheuvens, D.,
817   Schladitz, A., Schutz, L., and Weinbruch, S.: Electron microscopy of particles collected at Praia, Cape
818   Verde, during the Saharan Mineral Dust Experiment: particle chemistry, shape, mixing state and
819   complex refractive index, Tellus B, 63, 475-496, 2011.

820   Kim, J., Bauer, H., Dobovicnik, T., Hitzenberger, R., Lottin, D., Ferry, D., and Petzold, A.: Assessing
821   Optical Properties and Refractive Index of Combustion Aerosol Particles Through Combined
822   Experimental and Modeling Studies, Aerosol Sci. Technol., 49, 340-350, 2015.

823   Krämer, M. and Afchine, A.: Sampling characteristics of inlets operated at low U/U0 ratios: new
824   insights from computational fluid dynamics (CFX) modeling, J. Aerosol Sci, 35, 683-694, 2004.

825   Krejci, R., Strom, J., de Reus, M., and Sahle, W.: Single particle analysis of the accumulation mode
826   aerosol over the northeast Amazonian tropical rain forest, Surinam, South America, Atmos. Chem.
827   Phys, 5, 3331-3344, 2005.

828   Kumar, M. and Francisco, J. S.: Elemental sulfur aerosol-forming mechanism, Proc. Natl. Acad. Sci.
829   U.S.A., 114, 864-869, 2017.

830   Laskin, A. and Cowin, J. P.: Automated single-particle SEM/EDX analysis of submicrometer particles
831   down to 0.1 µm, Anal Chem, 73, 1023-1029, 2001.

832   Lee, K. W. and Ramamurthi, M.: Chapter 10: Filter Collection. In: Aerosol Measurement: Principles,
833   Techniques, and Applications

834   Willeke, K. and Baron, P. (Eds.), Van Nostrand Reinhold, New York, 1993.

835   Lindsley, W. G.: Filter Pore Size and Aerosol Sample Collection, NIOSH Manual of Analytical Methods,
836   2016. 1-14, 2016.

837   Liu, B. Y. H. and Ilori, T. A.: Aerosol deposition in turbulent pipe flow, Environ. Sci. Technol., 8, 351-
838   356, 1974.

839   Liu, B. Y. H., Zhang, Z. Q., and Kuehn, T. H.: A Numerical Study of Inertial Errors in Anisokinetic
840   Sampling, J. Aerosol Sci, 20, 367-380, 1989.

841   Lohmann, U. and Diehl, K.: Sensitivity Studies of the Importance of Dust Ice Nuclei for the Indirect
842   Aerosol Effect on Stratiform Mixed-Phase Clouds, J. Atmospheric Sci., 63, 968-982, 2006.

843   Lohmann, U. and Gasparini, B.: A cirrus cloud climate dial?, Science, 357, 248-249, 2017.

844   Mason, R. H., Si, M., Chou, C., Irish, V. E., Dickie, R., Elizondo, P., Wong, R., Brintnell, M., Elsasser, M.,
845   Lassar, W. M., Pierce, K. M., Leaitch, W. R., MacDonald, A. M., Platt, A., Toom-Sauntry, D., Sarda-
846   Esteve, R., Schiller, C. L., Suski, K. J., Hill, T. C. J., Abbatt, J. P. D., Huffman, J. A., DeMott, P. J., and
847   Bertram, A. K.: Size-resolved measurements of ice-nucleating particles at six locations in North
848   America and one in Europe, Atmos. Chem. Phys, 16, 1637-1651, 2016.

849   McConnell, C. L., Formenti, P., Highwood, E. J., and Harrison, M. A. J.: Using aircraft measurements to
850   determine the refractive index of Saharan dust during the DODO Experiments, Atmos. Chem. Phys,
851   10, 3081-3098, 2010.

852   McMurry, P.: A review of atmospheric aerosol measurements, Atmos. Environ., 34, 1959-1999, 2000.

853   Nakagawa, M. and Ohba, T.: Minerals in Volcanic Ash 1: Primary Minerals and Volcanic Glass, Global
854   Environ. Res., 6, 2003.

855 Nessler, R., Bukowiecki, N., Henning, S., Weingartner, E., Calpini, B., and Baltensperger, U.:
856 Simultaneous dry and ambient measurements of aerosol size distributions at the Jungfraujoch, Tellus
857 B, 55, 808-819, 2003.

858 Paciga, J. J., Roberts, T. M., and Jervis, R. E.: Particle-Size Distributions of Lead, Bromine, and Chlorine
859 in Urban-Industrial Aerosols, Environ. Sci. Technol., 9, 1141-1144, 1975.

860 Pratt, K. A., Mayer, J. E., Holecek, J. C., Moffet, R. C., Sanchez, R. O., Rebotier, T. P., Furutani, H., Gonin,
861 M., Fuhrer, K., Su, Y., Guazzotti, S., and Prather, K. A.: Development and characterization of an aircraft
862 aerosol time-of-flight mass spectrometer, Analytical Chemistry, 81, 1792-1800, 2009.

863 Pratt, K. A. and Prather, K. A.: Mass spectrometry of atmospheric aerosols--recent developments and
864 applications. Part II: On-line mass spectrometry techniques, Mass Spectrom. Rev., 31, 17-48, 2012.

865 Price, H. C., Baustian, K. J., McQuaid, J. B., Blyth, A., Bower, K. N., Choularton, T., Cotton, R. J., Cui, Z.,
866 Field, P. R., Gallagher, M., Hawker, R., Merrington, A., Miltenberger, A., Neely Iii, R. R., Parker, S. T.,
867 Rosenberg, P. D., Taylor, J. W., Trembath, J., Vergara-Temprado, J., Whale, T. F., Wilson, T. W., Young,
868 G., and Murray, B. J.: Atmospheric Ice-Nucleating Particles in the Dusty Tropical Atlantic, J. Geophys.
869 Res. Atmos., 123, 2175-2193, 2018.

870 Pruppacher, H. R. and Klett, J. D.: Microphysics of Clouds and Precipitation Dordrecht: Kluwer
871 Academic Publishers, 1997.

872 Pui, D. Y. H., Romay-Novas, F., and Liu, B. Y. H.: Experimental Study of Particle Deposition in Bends of
873 Circular Cross Section, Aerosol Sci. Technol., 7, 301-315, 1987.

874 Reid, E. A., Reid, J. S., Meier, M. M., Dunlap, M. R., Cliff, S. S., Broumas, A., Perry, K., and Maring, H.:
875 Characterization of African dust transported to Puerto Rico by individual particle and size segregated
876 bulk analysis, J. Geophys. Res. Atmos., 108, -, 2003.

877 Rosenberg, P. D., Dean, A. R., Williams, P. I., Dorsey, J. R., Minikin, A., Pickering, M. A., and Petzold, A.:
878 Particle sizing calibration with refractive index correction for light scattering optical particle counters
879 and impacts upon PCASP and CDP data collected during the Fennec campaign, Atmos. Meas. Tech., 5,
880 1147-1163, 2012.

881 Seinfeld, J. H. and Pandis, S. N.: Atmospheric Chemistry and Physics: From Air Pollution to Climate
882 Change, Wiley, 2006.

883 Soo, J. C., Monaghan, K., Lee, T., Kashon, M., and Harper, M.: Air sampling filtration media: Collection
884 efficiency for respirable size-selective sampling, Aerosol Sci Technol, 50, 76-87, 2016.

885 Talbot, R. W., Andreae, M. O., Berresheim, H., Artaxo, P., Garstang, M., Harriss, R. C., Beecher, K. M.,
886 and Li, S. M.: Aerosol Chemistry during the Wet Season in Central Amazonia - the Influence of Long-
887 Range Transport, J. Geophys. Res. Atmos., 95, 16955-16969, 1990.

888 Thomas, J. W.: Gravity Settling of Particles in a Horizontal Tube, J. Air Pollut. Control Assoc., 8, 32-34,
889 1958.

890 Thomson, D. S., Schein, M. E., and Murphy, D. M.: Particle Analysis by Laser Mass Spectrometry WB-
891 57F Instrument Overview, Aerosol Sci. Technol., 33, 153-169, 2000.

892 von der Weiden, S. L., Drewnick, F., and Borrmann, S.: Particle Loss Calculator – a new software tool
893 for the assessment of the performance of aerosol inlet systems, Atmos. Meas. Tech., 2, 479-494, 2009.

894 Wendisch, M. and Brenguier, J. L.: Airborne Measurements for Environmental Research: Methods and
895 Instruments, 2013.

896 Young, G., Jones, H. M., Darbyshire, E., Baustian, K. J., McQuaid, J. B., Bower, K. N., Connolly, P. J.,
897 Gallagher, M. W., and Choularton, T. W.: Size-segregated compositional analysis of aerosol particles
898 collected in the European Arctic during the ACCACIA campaign, Atmos. Chem. Phys, 16, 4063-4079,
899 2016.

900

901   **Figures**
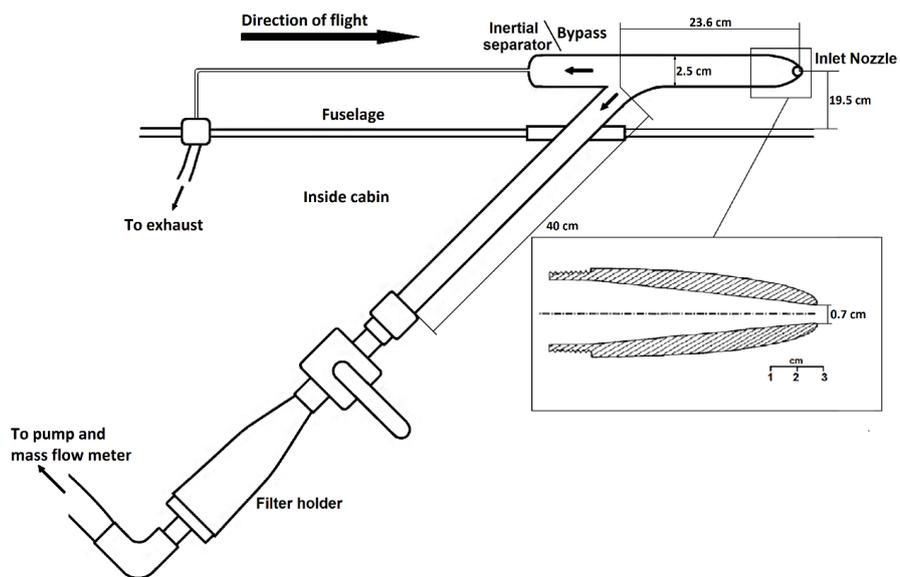
902

903   Fig. 1. Schematic diagram of one of the two parallel lines of the inlet system.

(a)

904

(b)

905

Atmospheric
Measurement
Techniques
Discussions

(c)
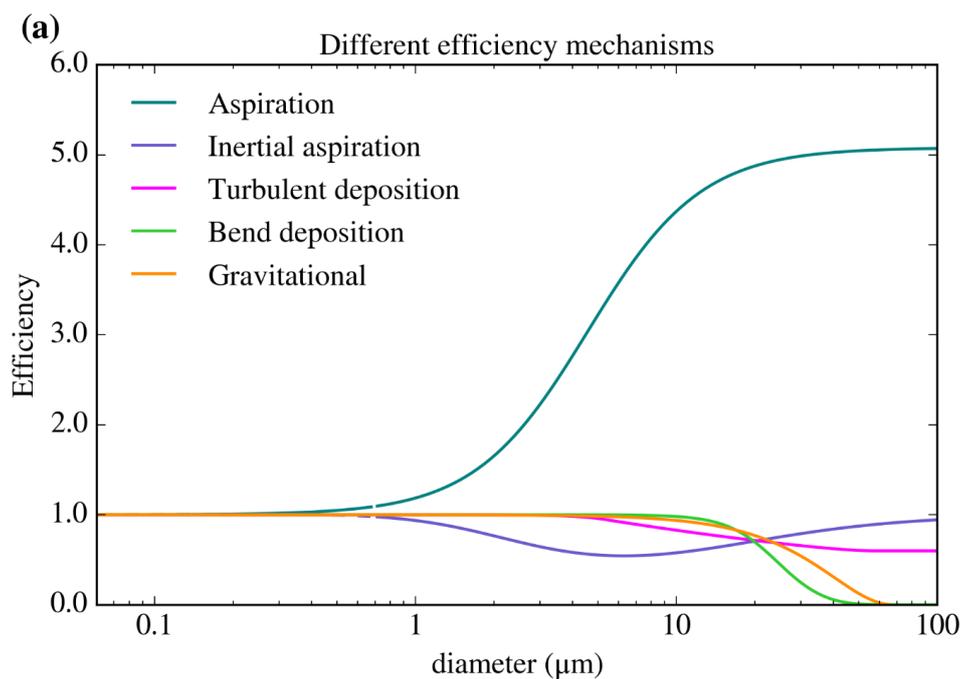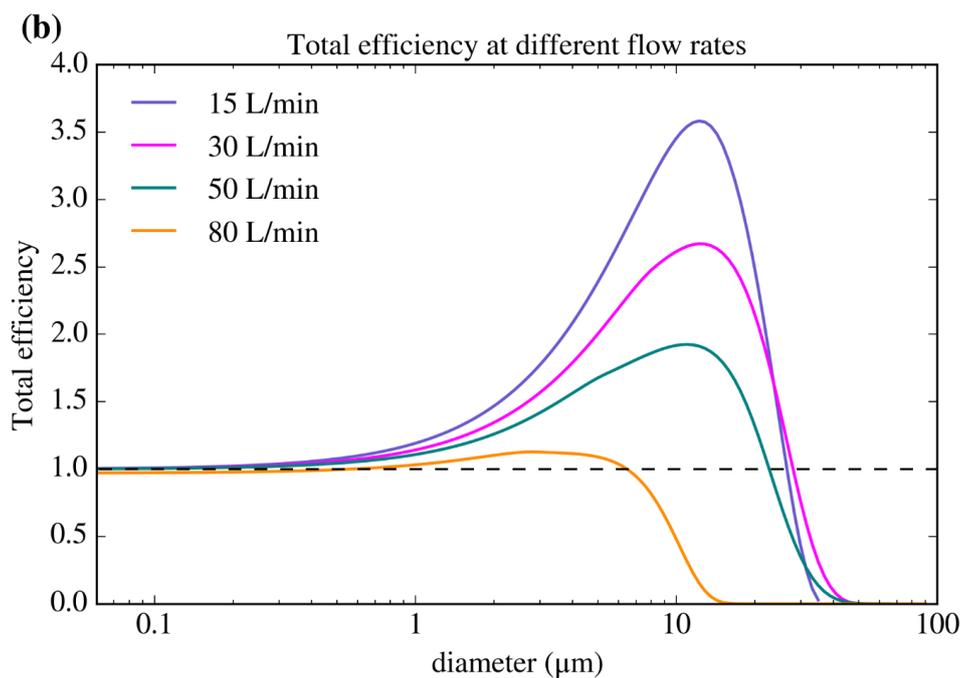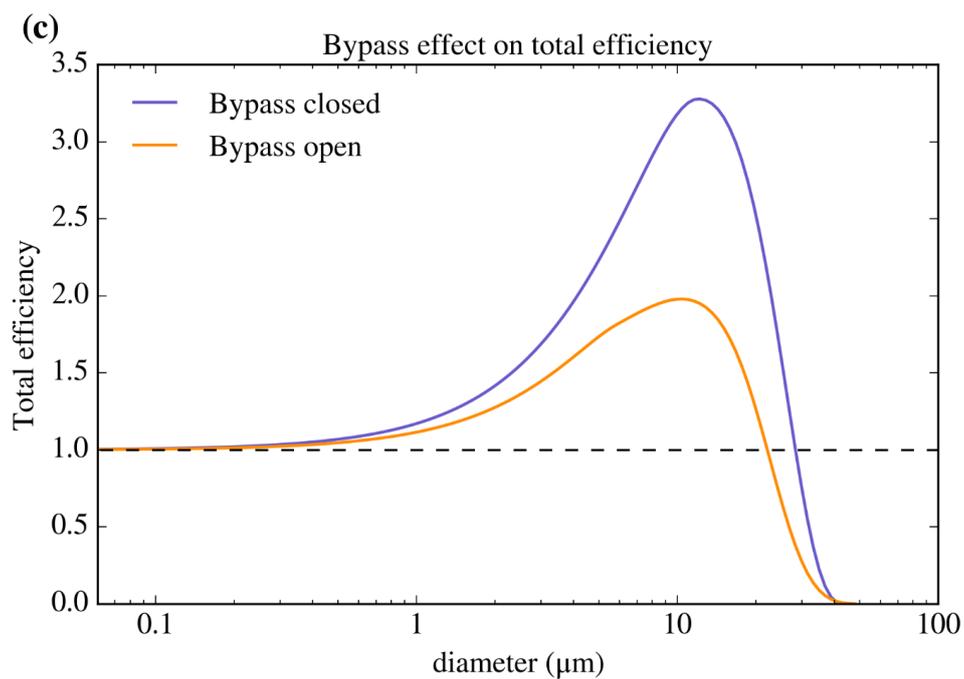
Fig. 2. *Theoretical efficiencies of the Filter inlet system.* (a) Efficiencies of the four mechanisms considered in this work for a total flow rate of 50 L min^{-1}. We have assumed a dynamic viscosity of 1.82x10^{-5} kg m^{-1} s^{-1} (value for 0 °C) and a particle density of 1000 kg m^{-3}. The speed of the air mass (U_0) was 110 m s^{-1}, a typical FAAM flying speed at low altitudes. (b) Total efficiency for four different total flow rates. For the 80 L min^{-1} case, turbulent deposition through the whole line was considered since the flow was turbulent through the whole pipe. (c) Total efficiency considering all the described mechanisms for a 20 L min^{-1} filter flow rate with the bypass closed and a 20 L min^{-1} filter flow rate with the bypass open (considering a bypass flow of 25 L min^{-1}).

915

(a)

(b)
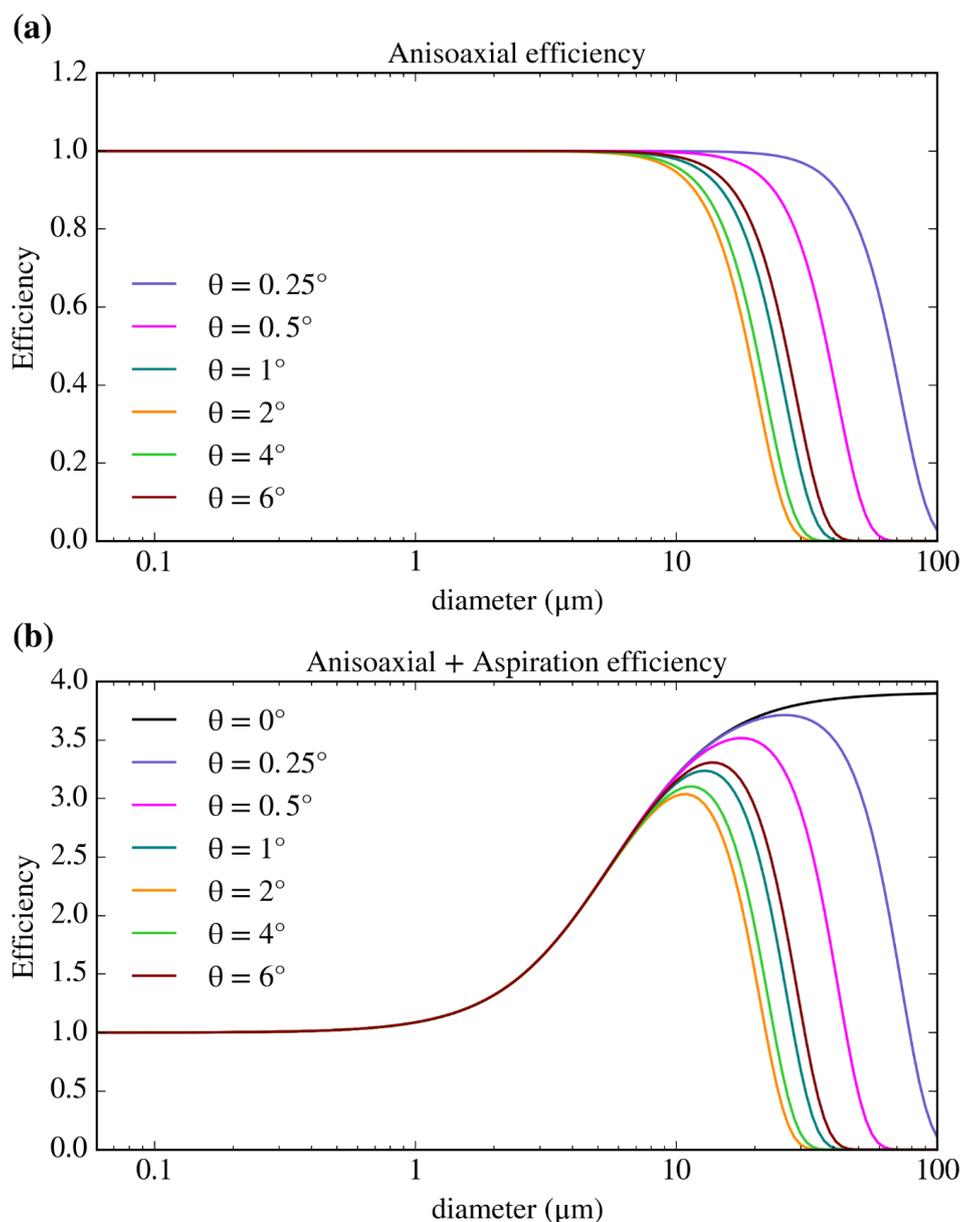
916
917 Fig. 3. Anisoaxial inertial losses of the sampling carried out by the Filters inlet system for different values of the angle in
918 between the inlet and the flight direction. The calculations have been presented by themselves (a) and combined with the
919 aspiration efficiency (b), which one can see in Fig. 2a. The anisoaxial calculations have been done using the equations given
920 by (Hangal and Willeke, 1990b), using the same parameters and dimensions than in Fig. 2, apart from the flow rate, which
921 was set to 65 L min^{-1} in order to be within the valid range of U/U_0 that was used to develop the equation. For smaller or
922 larger values of the flow rate (under which most of the sampling is carried out), the differences in the efficiency from the
923 ones show here are minimal.

924

925

926
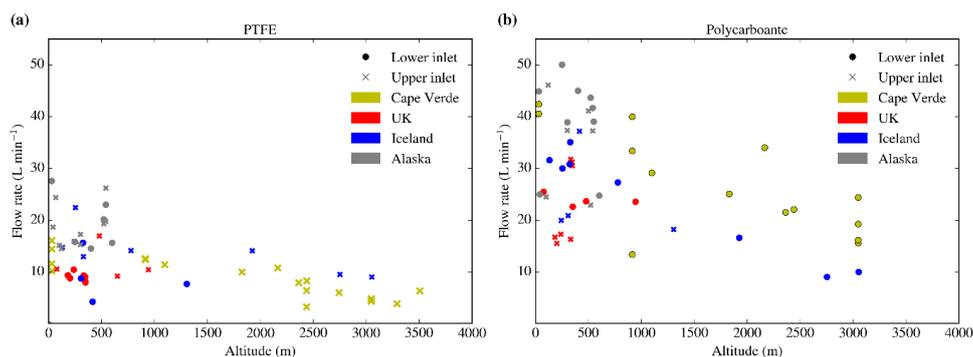
Figure 4. Filter flow rate of different samplings carried out in different campaigns at each altitude using: (a) Sartorius PTFE membrane filters (47mm diameter with a pore size of 0.45µm) and (b) Whatman nucleopore polycarbonate track etched filters (47mm diameter with a pore size of 0.4µm). The crosses represent samples taken in the upper line of the inlet system, whereas dots represent the sampling in the bottom line. Different mesh supports were used for the data collection. The data from Cape Verde was extracted from (Price et al., 2018) and the notes of the analysis carried out by the authors whereas the altitude data from the other three was obtained from the pressure altitude measurement carried out by the Reduced Vertical Separation Minimum system on board of the aircraft. The FAAM core datasets used (via the Centre for Environmental Data Analysis) were C019, C022, C024, C025, C058, C059, C060, C061, C062, C063, C085, C086, C087, C088, C089, C090 and C091. The bypass was closed for all the data in Cape Verde whereas it was open for all the data in the other campaigns. Note that the flow rate here corresponds to the filter flow rate (measured with the mass flow meter), not the total one.

937

Atmospheric
Measurement
Techniques
Discussions

938
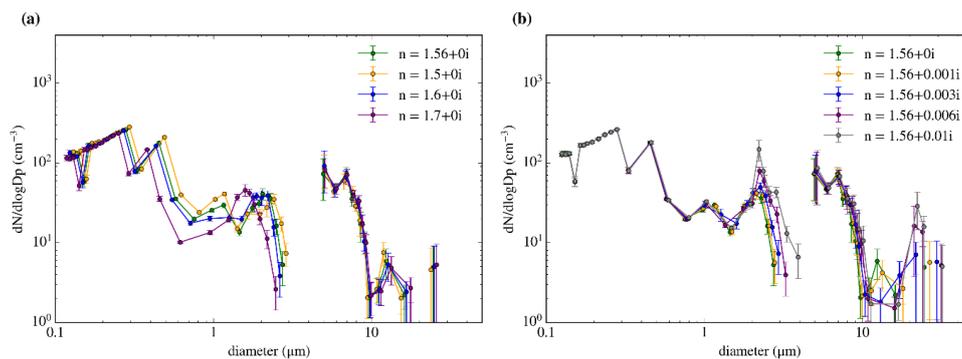
Figure 5. Sensitivity of the size distributions measured by the PCASP-CDP during the C010 flight on the 2017/05/10 from
11:24 to 11:38 UTC to small variations in the refractive index. We tested both the real part (a) and imaginary part (b). The
errors are calculated according to the methods explained in Sect. 3.

942

943
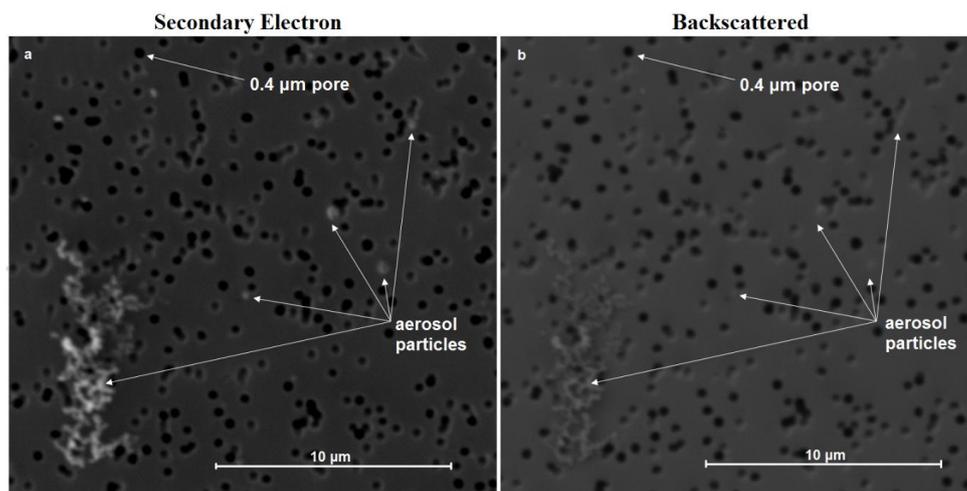
Figure 6. Secondary electron image (a) and Back Scattered Electron image (b) of the same area of the same filter, collected
on the 2018/07/05 from 13:32 to 13:47 in the upper line with the bypass open. As one can see, some of the small particles
in the SE image appear almost transparent under the BSE image. Even the 10μm soot particle in the bottom left of the
image shows a very low contrast in the BSE image.

948
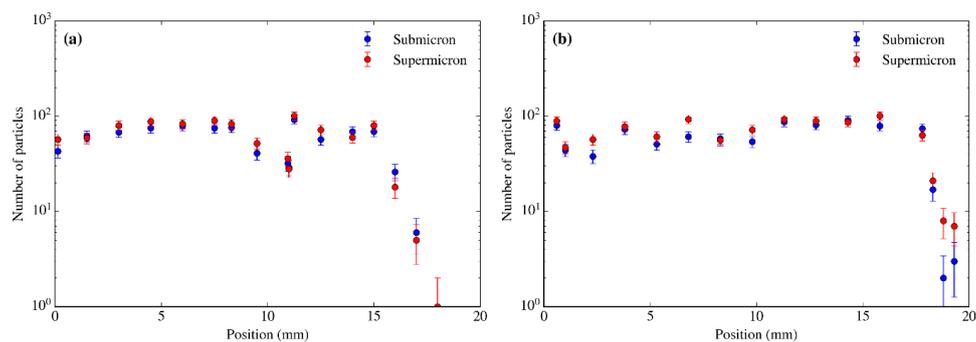
Figure. 7. Radial distribution of particles test on the sample collected on the 2017/10/02 from 16:24 to 16:40 UTC about 320 m high in south Iceland, using the lower line and open bypass, sampling 219 L. Number of submicron and supermicron particles in same size areas (~160x190 μm²) radially distributed versus the distance from the approximate centre through a radius of the filter (a) and another trajectory from the centre of the filter deviated 30° from the first radius (b). The analysis was done at 20 KeV and x5000. The number of both supermicron and submicron particles remains very constant all over the surface of the filter, until reaching the edges of it (which are cover by a rubber O-ring during the sample) and the number of particles drops to the limit of the detection within a few millimetres. The error in the number of particles comes from Poisson counting statistics.

Atmospheric
Measurement
Techniques
Discussions
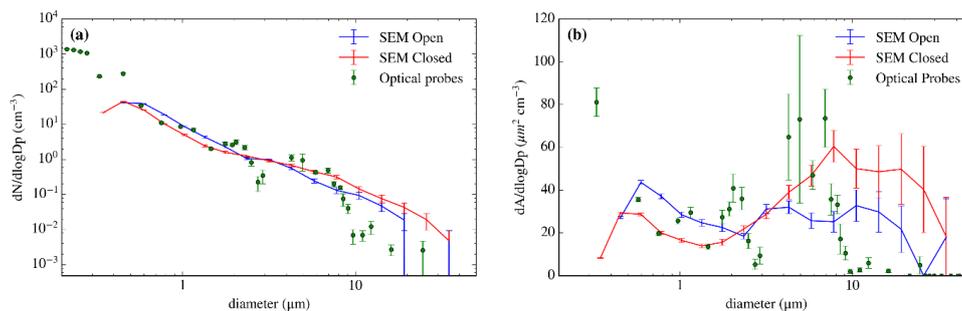
960
961 Figure 8. Bypass test carried out during the C010 flight on the 2017/05/10 from 11:24 to 11:38 UTC. The lower line sampled
962 226 L with the bypass closed, whereas the upper line sampled 141 L with the bypass open. The flow rates were 16.1 L min⁻¹
963 and 10.6 L min⁻¹ respectively. The optical probes are the PCASP-CDP, using the closest calibration to the sampling date and a
964 refractive index of 1.56 as stated in the Sect. 2.3. The data is shown in both number size distribution (a) and surface area size
965 distribution (b). The only error source considered for the SEM size distribution is the Poisson counting error, which has been
966 included this figure and all the subsequent figures including SEM size distributions.

967

Atmospheric
Measurement
Techniques
Discussions
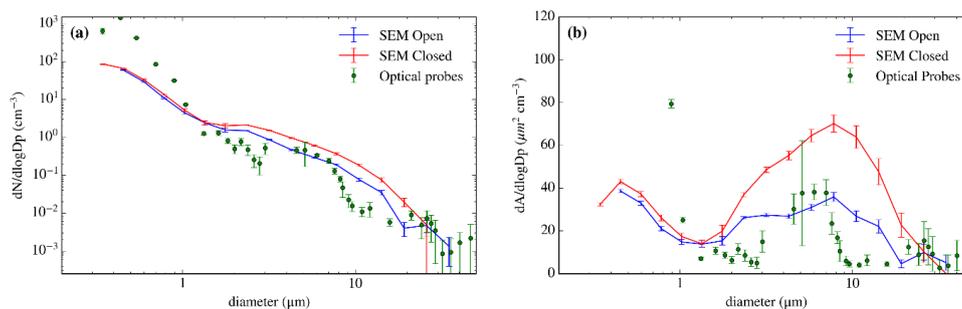
Figure 9. Bypass test carried out during the C057 flight on the 2017/09/27 from 13:33 to 13:50 UTC. The lower line sampled 555 L with the bypass open, whereas the upper line sampled 499 L with the bypass closed. The flow rates were 34.7 L min^{-1} and 31.2 L min^{-1} respectively. The position of the closed and open line was swapped with respect to the first analysis in Fig. 8. The optical probes are the PCASP-CDP, using the closest calibration to the sampling date and a refractive index of 1.56 as stated in the Sect. 2.3. The sampling was interrupted for a minute to avoid a turn.

Atmospheric
Measurement
Techniques
Discussions

976

977

978
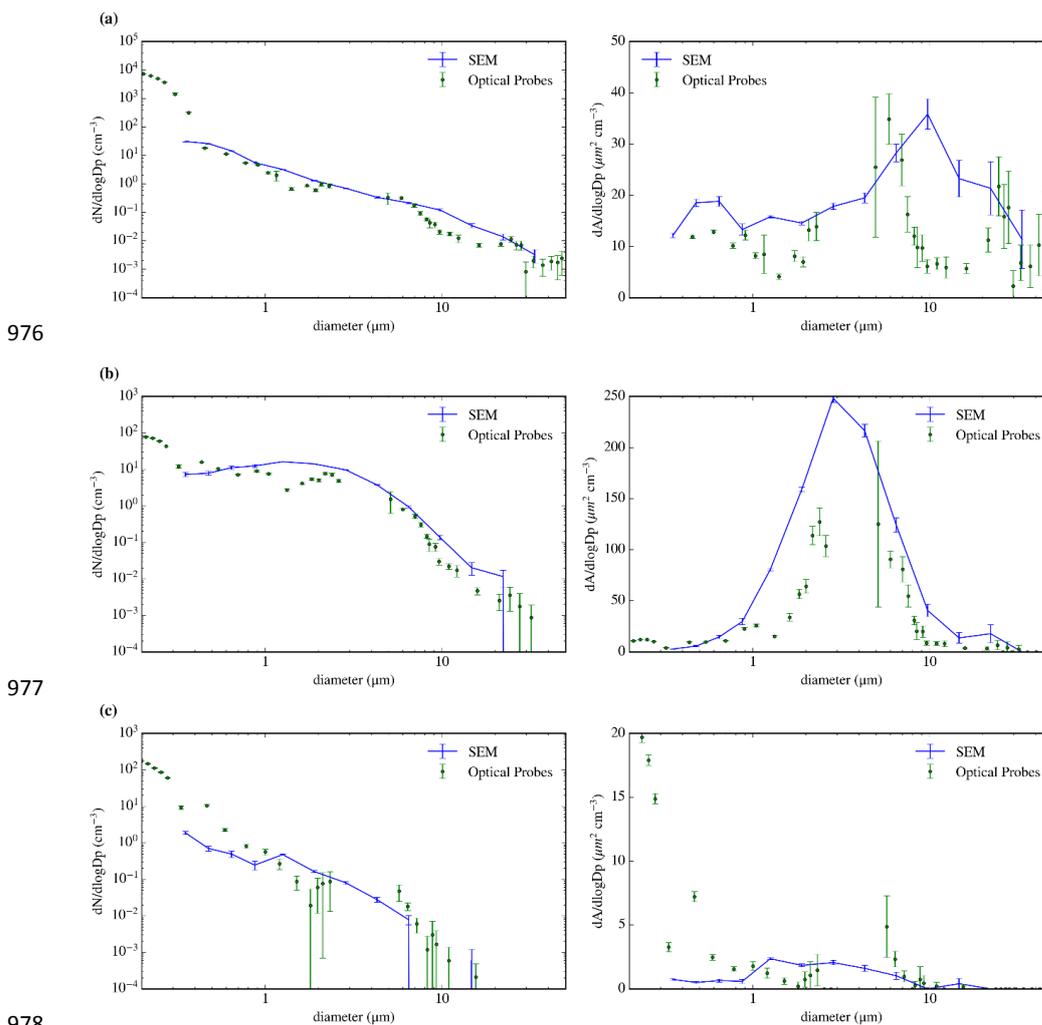
Figure 10. SEM obtained size distribution compared with PCASP-CDP online size distribution for three different sampling periods in three different aerosol environments. Close to London, on the 2017/07/19 from 15:20 to 15:51 UTC, sampling 953 L (a), south of Iceland on the 2017/10/02 from 16:24 to 16:40 UTC, sampling 432 L (b) and in north Alaska on the 2018/03/20 from 20:15 to 20:37, sampling 724 L (c). All the sampling was done in the upper line with the bypass open. The flow rates through the filter holders are 30.9, 30.5 and 42.0 L min^{-1} respectively. The optical probes are the PCASP-CDP, using the closest calibration to the sampling date and a refractive index of 1.56 as stated in Sect. 2.3.

985

(a)

(b)

986

987

Atmospheric
Measurement
Techniques
Discussions

Open Access

988
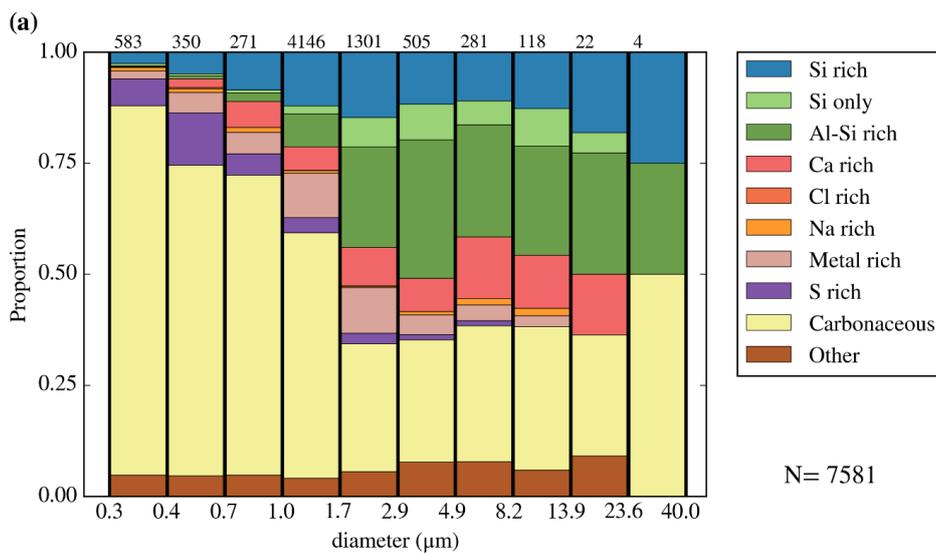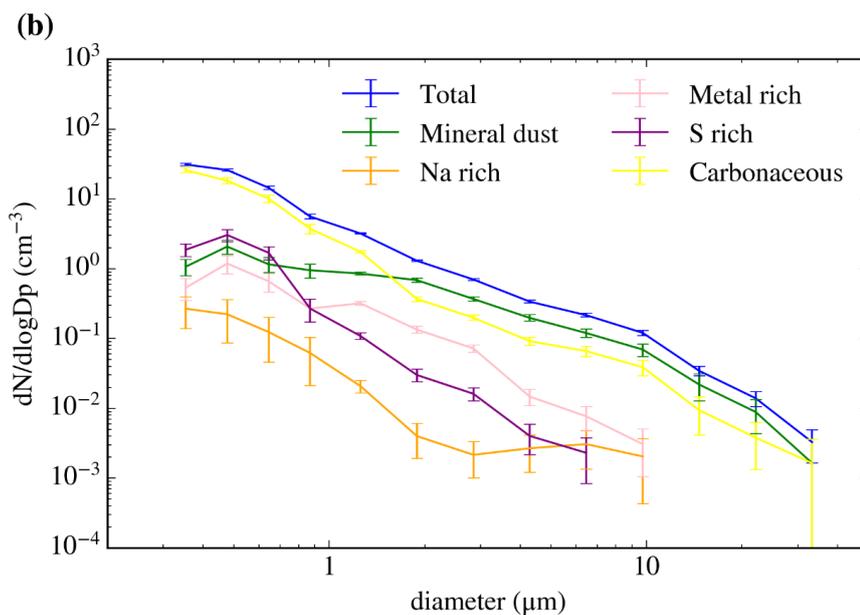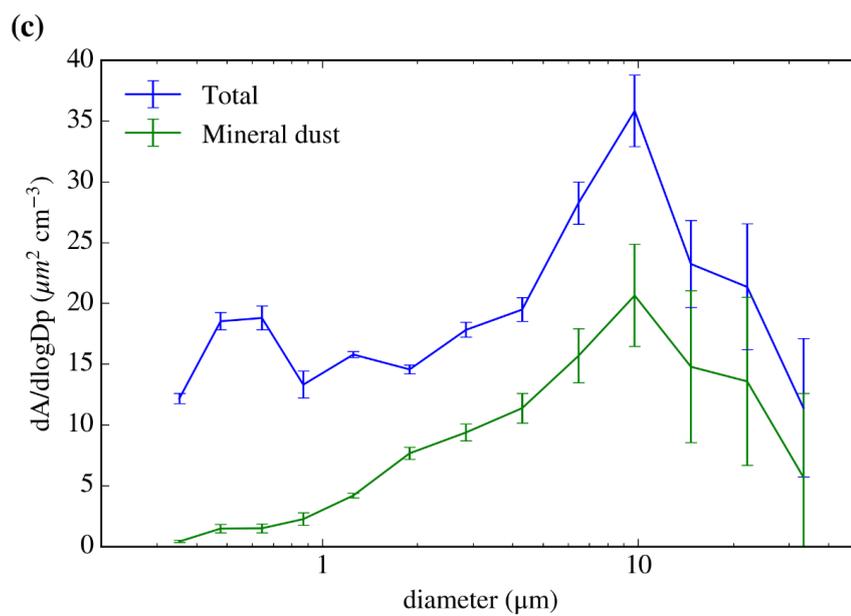
Fig. 11. Size-segregated compositional and morphological analysis of a sample collected close to London on the 2017/07/19
from 15:20 to 15:52 UTC by the lower line with the bypass open, sampling a total of 953L. (a) Fraction of particles
corresponding to each compositional category (described in the Sect. 7) for each size. The number of particles per bin can
be seen in the top of the figure. (b) Number size distribution for each composition. Cl rich particles were not included since
only two particles in this category were found. The errors have been calculated from the Poisson counting statistics (applying
it to both the size distribution and the compositional measurements). (c) Surface area of both all the detected aerosol
particles and the ones whose composition was consistent with mineral dust. Errors have been calculated in the same way as
before. By integrating the green curve in the figure (c) we obtained the total surface area of mineral dust in the sample (19.1
$\mu m^2\ cm^{-3}$).

998